Vertical Energy Fluxes Driven by the Interaction between Wave Groups and Langmuir Turbulence

MALCOLM E. SCULLY[a] AND SETH F. ZIPPEL[b]

[a] *Woods Hole Oceanographic Institution, Applied Ocean Physics and Engineering, Woods Hole, Massachusetts*
[b] *Oregon State University, College of Earth, Ocean, and Atmospheric Sciences, Corvallis, Oregon*

(Manuscript received 19 September 2023, in final form 17 March 2024, accepted 22 March 2024)

ABSTRACT: Data from an air–sea interaction tower are used to close the turbulent kinetic energy (TKE) budget in the wave-affected surface layer of the upper ocean. Under energetic wind forcing with active wave breaking, the dominant balance is between the dissipation rate of TKE and the downward convergence in vertical energy flux. The downward energy flux is driven by pressure work, and the TKE transport is upward, opposite to the downgradient assumption in most turbulence closure models. The sign and the relative magnitude of these energy fluxes are hypothesized to be driven by an interaction between the vertical velocity of Langmuir circulation (LC) and the kinetic energy and pressure of wave groups, which is the result of small-scale wave–current interaction. Consistent with previous modeling studies, the data suggest that the horizontal velocity anomaly associated with LC refracts wave energy away from downwelling regions and into upwelling regions, resulting in negative covariance between the vertical velocity of LC and the pressure anomaly associated with the wave groups. The asymmetry between downward pressure work and upward TKE flux is explained by the Bernoulli response of the sea surface, which results in groups of waves having a larger pressure anomaly than the corresponding kinetic energy anomaly, consistent with group-bound long-wave theory.

KEYWORDS: Langmuir circulation; Mixing; Oceanic mixed layer; Oceanic waves; Turbulence

1. Introduction

Breaking waves and Langmuir circulation (LC) are widely acknowledged to play an important role in the turbulence dynamics of the surface boundary layer of the ocean. Yet, exactly how these two processes result in elevated levels of turbulence near the ocean surface remains poorly understood. Quantifying turbulence is often accomplished by measuring the turbulent kinetic energy (TKE) dissipation rate ε, which in a constant stress layer adjacent to a rigid boundary layer is expected to follow "wall layer" scaling ($\varepsilon = u_*^3/\kappa z$), where u_* is the friction velocity, κ is von Kármán's constant, and z is the distance from the boundary. Most observations of ε made in the surface boundary layer of the ocean in the presence of waves are elevated relative to wall layer scaling. Terray et al. (1996) proposed a conceptual model for ε within the surface boundary layer under breaking waves. Their model consists of a near-surface breaking layer where ε is high and relatively uniform due to the surface flux of TKE by breaking waves F_{surf}, underlain by a wave-affected surface layer (WASL) where ε balances the vertical convergence in the downward energy flux.

Measurements made very near the ocean surface show that the dissipation within the near-surface breaking layer is not vertically uniform, with much higher dissipation rates under wave crests than wave troughs (Gemmrich 2010; Sutherland and Melville 2015b; Thomson et al. 2016). However, the intense dissipation rates measured above the mean height of the wave troughs are generally consistent with the concept of a near-surface breaking layer, where there is direct production of turbulence by wave breaking. Measurements of ε from the WASL show considerable variability. Many early studies documented values of ε that are consistent with wall layer scaling (Arsenyev et al. 1975; Soloviev et al. 1988). However, a growing number of studies present ε estimates in the WASL that significantly exceed wall layer scaling (Kitaigorodskii 1983; Agrawal et al. 1992; Anis and Moum 1995; Drennan et al. 1996; Terray et al. 1996; Sutherland and Melville 2015a; Scully et al. 2016). The Terray et al. (1996) scaling for ε in the WASL is a function of significant wave height H_s and F_{surf}, so that $\varepsilon = 0.3F_{\text{surf}}H_s z^{-2}$. The basic depth dependence of this scaling has been supported by some observational studies (Drennan et al. 1996; Feddersen et al. 2007; Jones and Monismith 2008; Gerbi et al. 2009). However, numerous other observations are inconsistent with this vertical form (Gargett 1989; Agrawal et al. 1992; Anis and Moum 1995; Huang and Qiao 2010; Thomson et al. 2016; Esters et al. 2018). Moreover, models commonly used to simulate the impact of wave breaking on near-surface turbulence (e.g., Craig and Banner 1994) include a much stronger vertical dependence ($\varepsilon \sim z^{-3.4}$). These previous studies highlight that no universal scaling for ε exists and that the exact mechanisms resulting in elevated turbulence in the WASL remain poorly understood.

Few observational studies have closed the TKE budget for the surface boundary layer under breaking waves. A notable exception was Scully et al. (2016) who made covariance measurements of the vertical energy flux and showed that its convergence balanced dissipation at first order. Their data demonstrated that the downward energy flux was driven primarily by the covariance between vertical velocity and pressure (e.g., pressure work). The energy flux driven by the

Denotes content that is immediately available upon publication as open access.

Corresponding author: Malcolm E. Scully, mscully@whoi.edu

DOI: 10.1175/JPO-D-23-0193.1

covariance of vertical velocity and TKE was upward, counter gradient to the direction assumed by nearly all turbulent closure models that include wave breaking. The downward energy flux in their data at $z \sim -2$ m was roughly 50% of the estimated wind energy input to the waves S_{in}, broadly consistent with the conceptual model proposed by Terray et al. (1996) for equilibrium conditions (i.e., $S_{in} = F_{surf}$). This correspondence between the wind input and downward energy flux led Scully et al. (2016) to conclude that processes driven by wave breaking must be responsible for the downward energy flux, but energetic LC was documented in the same dataset (Scully et al. 2015).

LC provides a potential mechanism that could transport TKE into, or produce TKE in, the WASL. Large-eddy simulations (LESs) suggest that enhanced dissipation results from Stokes production, the interaction between the Lagrangian Stokes drift shear and the vertical momentum flux (Polton and Belcher 2007; Kukulka et al. 2010). Other numerical simulations conclude that LC drives a convergence in the vertical energy flux and hence an increase in ε (Noh et al. 2004; McWilliams et al. 2012). Most numerical studies of LC do not include the influence of breaking waves despite the growing recognition that wave breaking provides the vertical vorticity that drives the LC instability (Csanady 1994; Teixeira and Belcher 2002; Sullivan et al. 2007). Even studies that account for wave breaking (Noh et al. 2004; Sullivan et al. 2007; Li et al. 2013) only do so in a relatively idealized way.

It is generally accepted that the interaction between the vertical Stokes drift shear and vorticity results in LC. The two most widely invoked mechanisms for the creation and maintenance of LC are 1) the distortion of spanwise vorticity by lateral gradients in Stokes drift [Craik–Leibovich direct-drive mechanism (CL1)] and 2) the tilting of vertical vorticity by the vertical Stokes drift shear [Craik–Leibovich instability mechanism (CL2)] (Leibovich 1983). Both mechanisms produce streamwise vorticity, with convergence developing under the downwind jet. The CL1 mechanism requires a fixed spatial pattern in Stokes drift typically associated with a bimodal directional wave spectra and the resulting crossed pattern of wave crests. It is viewed that this limits the generality of the CL1 mechanism, and the CL2 mechanism is more widely accepted as the primary driving mechanism for LC. However, nearly all numerical simulations of LC assume that the waves are unaffected by the circulations that they initiate. Given the difficulties simulating these feedbacks, most numerical simulations calculate the Stokes drift a priori and assume it has no spatial variability, other than in the vertical. Despite this assumption, ocean waves exhibit significant spatial variability, much of which is associated with wave groups. Wave groups are responsible for the horizontal energy flux and give rise to infragravity motions via group-bound long waves. Numerical studies ignore the interactions between LC and wave groups, arguing this approach is justified based on a clear separation of spatial scales (McWilliams et al. 2004).

Several theories involving feedbacks between surface waves and LC have been proposed. Garrett (1976) suggests that surface convergence, which is maximal in the downwind LC jet, amplifies wave amplitude and concentrates breaking in this region. In his conceptual model, preferential breaking in the convergent streaks enhances momentum transfer at these locations and generates vertical vorticity that is tilted over by the Stokes drift, resulting in positive feedback (e.g., CL2 mechanism). The model results of Smith (1983) contradict the conceptual model of Garrett (1976), demonstrating that wave reflection and refraction result in a decrease in wave amplitude at the center of a downwind jet, when the waves are propagating in the same direction as the jet. In his model, wave–current interaction not only decreases wave amplitude over the jet but also increases the local wavelength, decreasing wave steepness—which would decrease the likelihood of breaking in this region. These results are consistent with Veron and Melville (2001) who found that wave slope was reduced in regions of downwelling (e.g., the downwind jet) in laboratory experiments that simulated structures consistent with LC. They conclude that "waves that are initially generated by the wind are then strongly modulated by the Langmuir circulations that follow."

The recent numerical simulations of Fujiwara and Yoshikawa (2020) generally support the model results of Smith (1983) and emphasize the conclusions of Veron and Melville (2001). Their wave-resolving simulations explicitly account for the feedbacks between LC and wave propagation, negating the need to impose the spatial distribution of Stokes drift distribution. Their simulations suggest that LC refracts wave energy away from the downwind jet resulting in wave amplitude modulation in the crosswind direction. In their conceptual model, crosswind variations in Stokes drift associated with this amplitude modulation acting on the spanwise vorticity provide a source for streamwise vorticity—a more generally applicable mechanism to support the CL1 mechanism.

In this paper, we present data that suggest that the interactions between the vertical velocity of LC and the pressure/kinetic energy anomalies associated with wave groups play a fundamental role in vertical energy transport within the WASL. To support this assertion, we utilize field data collected from a fixed air–sea interaction tower deployed in Buzzards Bay, MA. These data are used to 1) close the near-surface TKE budget under energetic wind and wave forcing, 2) resolve the structure of group-bound long waves and compare these observations to the theoretical model of Longuet-Higgins and Stewart (1962) (hereafter LHS62), and 3) document the presence and importance of LC. The theoretical background, including the model of LHS62, is presented in section 2, and the data and experimental details are described in section 3. The analytical methods are described in section 4, and the results of this analysis are presented in section 5. We hypothesize that deviations in vertical velocity from the LHS62 solution, which drive the observed energy fluxes, are the results of wave–current interaction like that proposed by Smith (1983) and Fujiwara and Yoshikawa (2020). Evidence for this interaction and its implications is discussed in section 6.

2. Theoretical background

A primary goal of this analysis is to quantify the TKE balance in the upper ocean under energetic wave forcing, which

for steady and horizontally uniform flow can be represented as

$$-\overline{u_i'w'}\frac{\partial \overline{U_i}}{\partial z} - -\overline{u_i'w'}\frac{\partial \overline{U_s}}{\partial z} - \frac{g}{\rho_0}\overline{\rho'w'} - \frac{\partial}{\partial z}\left(\frac{1}{2}\overline{u_j^{i2}w'} + \frac{1}{\rho_0}\overline{p'w'}\right) = \varepsilon, \tag{1}$$

where the overbars and primes indicate Reynolds averages and deviations, respectively. The index i includes the two horizontal velocity components (u,v), and the index j includes all three components of velocity, including the vertical velocity w. The terms on the lhs are production by the mean Eulerian shear $(\partial\overline{U_i}/\partial z)$, production by the Lagrangian Stokes drift shear $(\partial\overline{U_s}/\partial z)$, buoyancy flux, and the divergence in vertical transport. The vertical transport includes both the TKE flux (first term inside parentheses) and the pressure work (second term inside parentheses).

At frequencies lower than the dominant surface waves, variations in pressure and kinetic energy are dominated by wave groups. Groups of waves with varying amplitude a are ubiquitous in the ocean and arise from interactions between waves of different frequencies σ. Wave energy $(E = 1/2\rho g a^2)$ is carried by the wave groups at the group velocity C_g, which can be derived from linear theory as $C_g = \partial\sigma/\partial k$, where k is the wavenumber of the dominant surface waves. The Bernoulli response to variations in wave kinetic energy associated with wave groups gives rise to low-frequency group-bound long waves. The high kinetic energy/low pressure under large wave groups results in a setdown of the mean sea surface, and the low kinetic energy/high pressure associated with small groups of waves drives a setup of the mean sea surface. This pattern of sea surface setup/setdown, which has a wavelength much longer than the primary surface waves, propagates with the wave groups at the group velocity (hence the term group-bound long wave). LHS62 derive a solution for group-bound long waves using the perturbation method of Stokes. For a narrow distribution of frequencies, and at time scales longer than the primary surface waves, LHS62 assume that the wave amplitude squared (e.g., the group energy) can be represented as the summation:

$$a^2 = \sum_{n,m} a_n a_m \cos(\Delta kx - \Delta\sigma t), \tag{2}$$

where terms associated with the individual waves average to zero and only the difference terms are retained. With this assumption, LHS62 derive a second-order solution for the velocity potential ϕ_2 that describes group-bound waves in water depth h that arise from differences in the wavenumber Δk and frequency $\Delta\sigma$ of the primary surface waves:

$$\phi_2 = -K\sum_{m,n}\frac{a_m a_n C_g}{gh\theta - C_g^2}\frac{1}{\Delta k}\frac{\cosh[\Delta k(z+h)]}{\cosh[\Delta kh]}\sin(\Delta kx - \Delta\sigma t), \tag{3}$$

with coefficients

$$K = \frac{\sigma^2}{4\sinh^2(kh)}\frac{\sinh(4kh) + 3\sinh(2kh) + 2kh}{\sinh(2kh) + 2kh} \quad \text{and} \tag{4}$$

$$\theta = \frac{\tanh(\Delta kh)}{\Delta kh}. \tag{5}$$

The term proportional to $(gh\theta - C_g^2)^{-1}$ is different for each wave frequency in the summation, but LHS62 present a solution for the simple case where only two sinusoidal wave components are present. In this case,

$$a^2 = (a_1^2 + a_2^2) + 2a_1a_2\cos(\Delta kx - \Delta\sigma t). \tag{6}$$

Here, the subscripts are used to indicate the two wave components (not the order of the solution). The first term inside the parentheses on the rhs of (6) is simply a constant with no time variation associated with the wave groups. Since we are only interested in the time-varying part, we define $\Delta a^2 = 2a_1a_2$ as the time-varying energy of the group wave envelope. For the simple case of only two waves interacting, the summation is not necessary and Eq. (3) can be written as

$$\phi_2 = -K\Delta a^2\left\{\frac{C_g}{gh\theta - C_g^2}\frac{1}{\Delta k}\frac{\cosh[\Delta k(z+h)]}{\cosh[\Delta kh]}\right\}\sin(\Delta kx - \Delta\sigma t). \tag{7}$$

The basic properties of the long wave, including the sea surface elevation η_2, horizontal velocity u_2, vertical velocity w_2, and pressure P_2, are derived from (7) as follows:

$$g\eta_2 = -\left(\frac{\partial\phi_2}{\partial t} + \frac{1}{2}\mathbf{u}_1^2 + \eta_1\frac{\partial}{\partial z}\frac{\partial\phi_1}{\partial t}\right) = -\Delta a^2\left[K\frac{C_g^2}{gh\theta - C_g^2} + \frac{\sigma^2}{4\sinh^2(kh)}\right]\cos(\Delta kx - \Delta\sigma t), \tag{8}$$

$$u_2 = \frac{\partial\phi_2}{\partial x} - K\Delta a^2\frac{C_g}{gh\theta - C_g^2}\frac{\cosh[\Delta k(z+h)]}{\cosh[\Delta kh]}\cos(\Delta kx - \Delta\sigma t), \tag{9}$$

$$w_2 = \frac{\partial\phi_2}{\partial z} - K\Delta a^2\frac{C_g}{gh\theta - C_g^2}\frac{\sinh[\Delta k(z+h)]}{\cosh[\Delta kh]}\sin(\Delta kx - \Delta\sigma t), \tag{10}$$

$$\frac{P_2}{\rho} = -\left(\frac{\partial\phi_2}{\partial t} + \frac{1}{2}\mathbf{u}_1^2\right) = -\Delta a^2\left\{K\frac{C_g^2}{gh\theta - C_g^2}\frac{\cosh[\Delta k(z+h)]}{\cosh[\Delta kh]} + \sigma^2\frac{\cosh[2k(z+h)]}{4\sinh^2(kh)}\right\}\cos(\Delta kx - \Delta\sigma t). \tag{11}$$

This set of equations provides a kinematic description of group-bound long waves, which dynamically are forced by variations in kinetic energy associated with wave groups. An important aspect predicted by this solution is that the pressure anomaly is larger than the kinetic energy anomaly because the pressure includes contributions from the sea surface setup. Additionally, the pressure anomaly decreases less rapidly with depth $\{\sim\cosh[\Delta k(z+h)]/\cosh[\Delta kh]\}$ than the kinetic energy anomaly $\{(\sim\cosh[2k(z+h)]/4\sinh^2[kh]\}$.

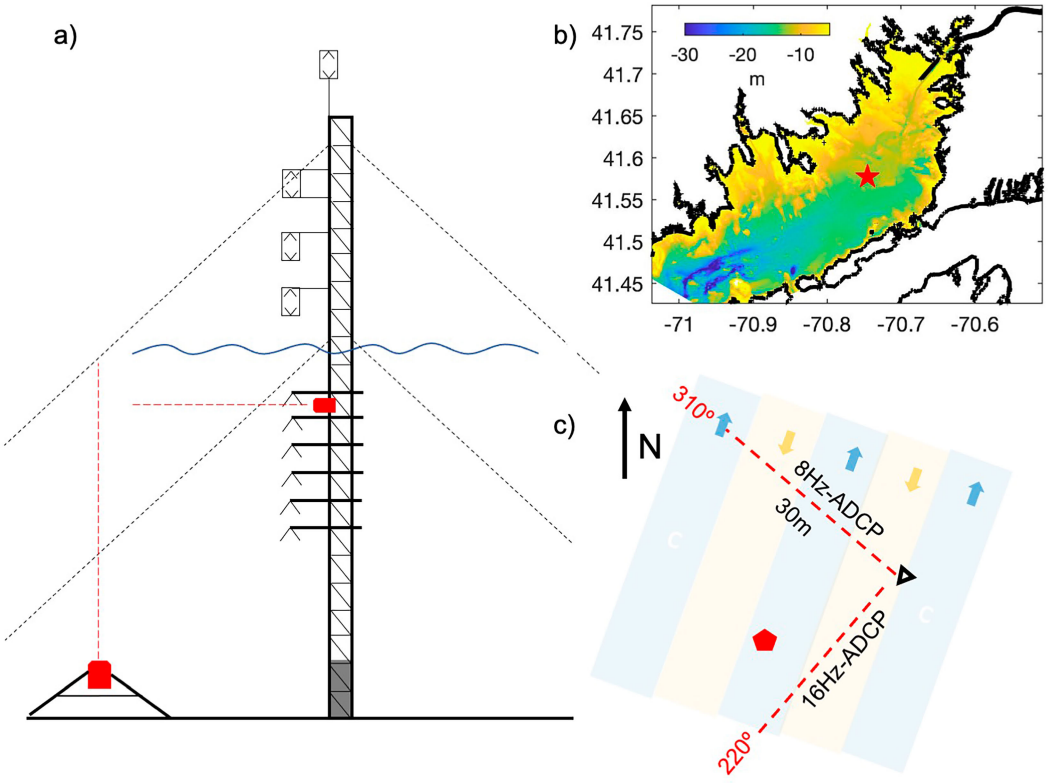

FIG. 1. (a) Schematic of the Buzzards Bay air–sea interaction tower depicting the vertical positions of the 6 ADVs, 4 sonic anemometers, 2 horizontal-looking ADCPs at $z \sim -3.5$ m, and adjacent bottom-mounted upward-looking ADCP; (b) site map and bathymetry (in meters) of the tower location in Buzzards Bay, MA; and (c) plan view of the tower orientation, including the relative positions of upward-looking ADCP (red pentagon) and the fifth beam (30-m range with 0.5-m bins) of the 8- and 16-Hz horizontal ADCPs. The 8-Hz ADCP was oriented toward 310°N, in line with the orientation of the ADVs, and the 16-Hz ADCP was oriented toward 220°N. The colored strips and associated arrows in inset (c) depict the approximate orientation of the Langmuir windrows and their velocity during the short deployment of the horizontal-looking ADCPs (11–12 Nov 2022). For both horizontal ADCPs, positive along-beam velocity is defined as toward the ADCP/tower.

3. Observations

The focal point of this analysis is the data collected from an air–sea interaction tower deployed in Buzzards Bay, MA (Zippel et al. 2024). The tower is a commercially available (Rohn Industries) telecommunication tower with a triangular cross section and open lattice design. The total tower height was ~21 m and was deployed where the mean water depth was ~13 m in a region of relatively uniform bathymetry (Fig. 1). The tower was supported by six guy wires attached to three anchors, which held the tower vertical providing a stable platform from which to make both atmospheric and oceanic covariance fluxes. The oceanographic instruments of primary interest to this analysis are a vertical array of six acoustic Doppler velocimeters (ADVs) that were evenly spaced (Δz ~1.1 m) from ~1.8 to ~7.2 m below the mean water surface. Each ADV was mounted on a pole that extended out ~1.3 m from the tower along a heading of 310°N, roughly perpendicular to the primary axis of fetch [e.g., southwest (SW)/northeast (NE)]. Each ADV measured three-dimensional velocity at 32 Hz and was coupled to an analog Keller pressure sensor that was sampled synchronously with velocity. Each pressure sensor was equipped with a small metal tube whose end was immediately adjacent to the ADV sampling velocity to provide collocated (<2 cm) covariance measurements of pressure and velocity.

Several additional instruments were deployed to complement the ADV measurements. The thermal structure of the water column was measured by a vertical array of 12 RBR thermistors that sampled continuously at 1 Hz with a vertical spacing of ~0.5 m spanning the upper ~8 m of the water column. Four CTDs were deployed at ~0.5, 3.8, 5.9, and 7.7 m from the mean water surface to characterize the density structure. A 1-MHz Nortek 5-beam acoustic Doppler current profiler (ADCP) was deployed in a bottom frame ~20 m southwest of the tower. This upward-looking ADCP sampled continuously at 4 Hz providing both high-frequency velocity and acoustic backscatter data in 0.5-m vertical bins over the entire duration of the experiment. The ADCP also collected high-resolution echo sounder data with 1.2-cm vertical resolution, also at 4 Hz. This echo sounder data resolved the sea surface with centimeter-scale resolution, providing high-quality

estimates of the sea surface over the entire duration of the experiment (used for wave statistics).

To complement these long-term observations, a short-term deployment with two additional 1-MHz Nortek 5-beam ADCPs was conducted. These two additional ADCPs were mounted to the tower by divers in a horizontal-looking orientation roughly 3.5 m below the mean water surface. Only the fifth beam was sampled, collecting along-beam velocity and acoustic backscatter over 59 0.5-m bins, covering a horizontal range of ~30 m at a constant depth. One ADCP which sampled at 16 Hz was pointed outward from the tower on a heading of 220°N. The other ADCPs sampled at 8 Hz on a heading of 310°N. We will refer to these two orthogonally oriented instruments as the 16- and 8-Hz ADCPs in the analysis below. Both ADCPs sampled continuously and were deployed on 11 November 2022, in anticipation of a strong forecasted wind event. Without an external battery housing, these ADCPs only sampled for ~48 h before the internal batteries failed. In addition to these water-side instruments, the tower collected a suite of vertically resolved atmospheric measurements (see Zippel et al. 2024, for details), but they will not be presented here.

The tower and associated instruments were deployed from 12 April to 13 June 2022, and again from 21 September to 13 December 2022, although not all instruments sampled for the entirety of each deployment. During the spring deployment, the velocity data from the uppermost ADV exhibited excessive noise and very low signal-to-noise ratios, and the ADV located at $z \sim -4.6$ m failed on 8 May. Given these issues with the first deployment, this analysis will focus exclusively on the second deployment for the period from 21 September to 19 November 2022—the period when complete data from most of the ADVs are available.

4. Analysis

The ADVs collected 20 min of data every half hour over the course of the experiment and provided all the necessary data to evaluate Eq. (1). Reynolds averaging was performed on these bursts with turbulent quantities defined as the deviations from the linearly detrended 20-min data, providing statistically stationary data consistent with the steady-state assumption in Eq. (1). Consistent with the methods of Scully et al. (2016), the turbulent momentum flux was calculated by integrating the horizontal and vertical velocity cospectra over frequencies lower than the dominant surface waves (<1/15 Hz). Momentum flux estimates from the uppermost ADV agree favorably with atmospheric estimates made from the lowest sonic anemometer (data not shown). The vertical energy fluxes were calculated in a similar manner, but the integration of cospectra of vertical velocity and TKE/pressure was limited to frequencies > 1/200 and <1/15 Hz. Including lower frequencies results in energy fluxes that are noisier but does not change the basic results presented below. Estimates of ε were made from the height of the inertial subrange of vertical velocity for frequencies higher than the observed surface waves (>1 Hz). The vertical velocity autospectra and the corresponding estimates of ε were adjusted following the method of Gerbi et al. (2009), which accounts for spectral distortion caused by the unsteady advection of turbulence by wave motions (Lumley and Terray 1983).

A primary goal of this analysis is to compare the observed low-frequency (<1/15 Hz) velocity and pressure to the LHS62 solution for group-bound long waves. To that end, the velocity data were first rotated into the direction of wave propagation, defined based on the dominant wave direction where u, v, and w represent the along-wave, across-wave, and vertical velocities, respectively. Velocity and pressure were then detrended and low-pass filtered to remove frequencies above 1/15 Hz. To isolate the measured variability associated with the group-bound long waves, the data are then averaged as a function of the long-wave phase Θ_{LW}, which is defined in terms of the group envelop η_{env} of the observed surface waves:

$$\eta_{env} = |H\{\eta\}|, \tag{12}$$

where $H\{\cdot\}$ indicates the Hilbert transform. We use the uppermost pressure sensor to estimate η. Following Longuet-Higgins (1984), this near-surface pressure is bandpass filtered with cutoffs of 1.5 and 0.5 times the peak wave frequency (obtained from ADCP sea surface) to isolate the dominant waves contributing to the wave group. With this estimate of the group envelop, the long-wave phase Θ_{LW} is estimated from the real and imaginary parts of the Hilbert transform of the demeaned values of η_{env}:

$$\Theta_{LW} = \tan^{-1}(\text{real}\{H\{\eta_{env}\}\}, \text{imag}\{H\{\eta_{env}\}\}). \tag{13}$$

Based on this definition, $\Theta_{LW} = 90°$ under the high groups of waves and $\Theta_{LW} = -90°$ under the low groups (see below). Estimates of η_{env} also are used to define the amplitude squared of the wave groups so that $\Delta a^2 = \eta_{env}^2$. Since we are only interested in the time-varying component of the solution and not the mean current, the mean value of Δa^2 is removed for all calculations. Evaluating the model of LHS62 also requires characterization of the dominant surface waves (k, σ, and C_g) and estimates of the group wavelength (e.g., Δk). Estimates of k, σ, and C_g are derived from linear wave theory using the observed water depth and the peak wave period calculated from spectra of ADCP sea surface elevation. The group wavelength is estimated simply as

$$\Delta k = \frac{2\pi \#_g}{\Delta t C_g}, \tag{14}$$

where Δt is the duration of the burst (i.e., 20 min), C_g is the group velocity derived from linear wave theory, and $\#_g$ is the number of wave groups defined as the number of upcrossings where $\eta_{env} > 2/3 H_{sig}$.

5. Results

a. Overview of experiment

This analysis focuses on the fall deployment from 22 September to 19 November 2022. During this period, there were several energetic wind events with wind speed exceeding 8 m s^{-1}

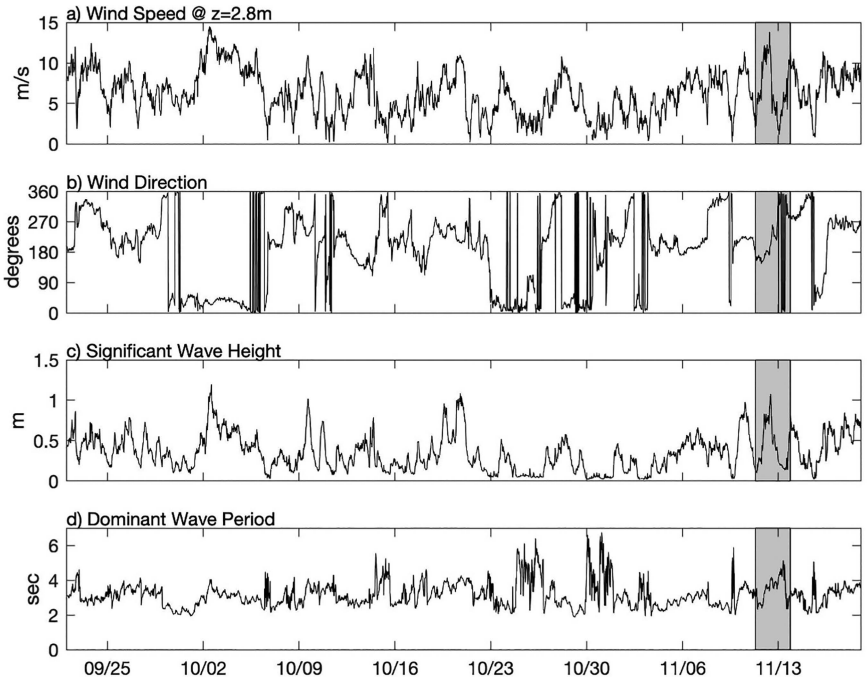

FIG. 2. Overview of the wind and wave forcing observed during the fall 2022 deployment including (a) wind speed measured at the lowest sonic anemometer ($z \sim 2$ m), (b) wind direction, (c) significant wave height, and (d) dominant wave period. Wave statistics were derived from the sea surface elevation inferred from the high-resolution (1.2 cm) echo intensity data measured by the upward-looking ADCP, which were sampled at 4 Hz. The shaded gray regions indicate the time of the horizontal-looking ADCP deployment in mid-November.

(Fig. 2). The H_s reached ~1 m during moderate wind forcing, and the mean wave period was 3.8 s, consistent with fetch-limited waves. During weak local wind forcing, remote swell from the SW was detected at the tower location, but this only accounted for a significant fraction of wave energy when $H_s < 0.2$ m. Tidal currents in Buzzards Bay are relatively weak, typically less than 0.1 m s^{-1}, and estimates of bottom stress were ~15 times smaller than those of the surface stress during the strong wind forcing conditions considered below. As a result, turbulence generated in the bottom boundary layer is not expected to contribute significantly to the upper half of the water column that is the focus of this analysis. During conditions of weak wind forcing, thermal stratification developed, but the water column was well-mixed when wind speeds exceeded ~6 m s^{-1}.

b. *Turbulent kinetic energy balance*

We are interested in conditions with strong wind/wave forcing, so we evaluate the terms in the TKE balance for conditions when the measured wind speed was greater than 8 m s^{-1}. At the uppermost ADV ($z \sim -1.8$ m), ε exceeds shear production by nearly a factor of 20 (Fig. 3) and the integrated shear production is more than an order of magnitude smaller than the integrated dissipation during energetic conditions (Fig. 4). The shear production term exceeds the Stokes production at all the ADV locations other than the uppermost pair, and the integrated Stokes production across the ADV array is roughly five times smaller than the integrated shear production. Consistent with the results of Scully et al. (2016), the net energy flux is downward and the convergence in this flux balances the estimated dissipation throughout the resolved portion of the water column. Although the net energy flux is directed downward, the pressure work is directed downward and the kinetic energy flux is directed upward (Fig. 5). The net downward flux occurs because the magnitude of the pressure work exceeds the kinetic energy flux by a factor of ~3 near the surface and by as much as a factor of ~30 at depth.

Combined with the results of Scully et al. (2016), these data provide a second dataset and different geographic location where the first-order TKE balance under breaking waves is closed. Both datasets document that elevated dissipation rates in the WASL result from the vertical convergence in vertical energy flux, consistent with commonly assumed conceptual models (e.g., Craig and Banner 1994; Terray et al. 1996). However, there is an important but subtle distinction from these models; mechanistically, the convergence in the downward energy flux is driven by pressure work, and the TKE flux is upward (counter gradient) and divergent. Scully et al. (2016) hypothesized that the downward pressure work was somehow related to wave breaking, but we explore an alternate hypothesis below.

c. *Group-bound long waves*

The covariance energy fluxes presented above were calculated from frequencies where there are significant pressure

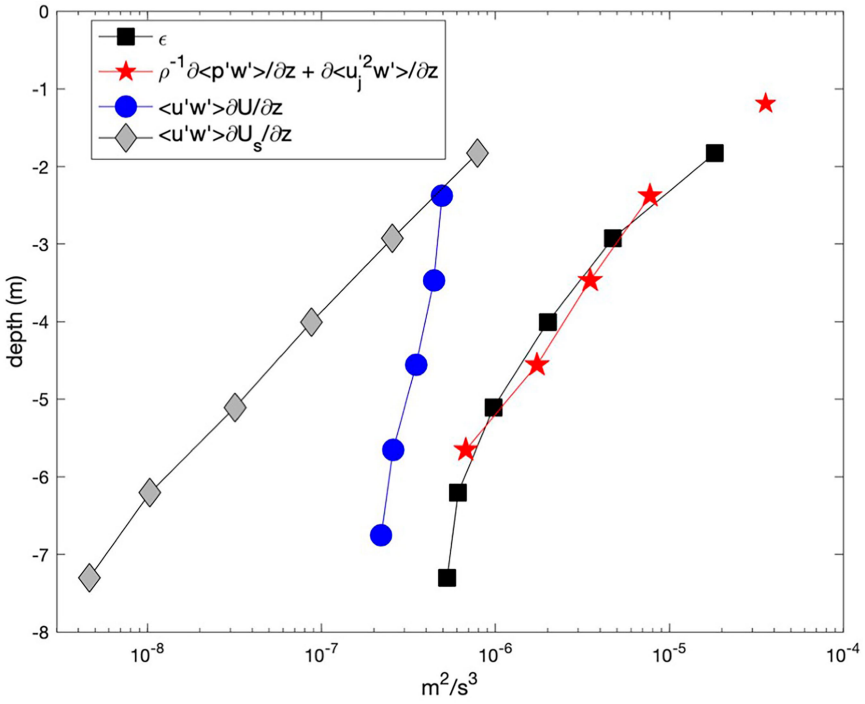

FIG. 3. Vertical profiles of the terms in the TKE budget including turbulent dissipation rate (black squares), convergence in vertical energy flux including both pressure work and TKE transport (red stars), shear production (blue circles), and Stokes production (gray diamonds). The profiles are obtained by averaging all data for conditions where the wind speed was greater than 8 m s^{-1} to isolate conditions with strong forcing and wave breaking. The convergence in vertical energy flux and shear production terms involve differences between adjacent ADVs (resulting in five vertical locations). An additional estimate of the convergence in vertical energy flux is obtained by differencing the measured energy flux at the upper ADV and the estimated wind input at the surface following Plant (1982). Consistent with Scully et al. (2016), the dominant TKE balance is between the convergence in vertical energy flux and turbulent dissipation.

and kinetic energy fluctuations associated with wave groups. Furthermore, the increasing magnitude of downward pressure work relative to upward kinetic energy flux with increasing depth suggests that the physical processes driving energy flux are related to the energy associated with wave groups. It is therefore instructive to compare the pressure and velocity data collected at the tower to the group-bound long-wave theory of LHS62 (Fig. 6). As with the TKE budget, we restrict our analysis to energetic conditions when wind speeds exceed 8 m s^{-1}. Averaged in this way, the horizontal velocity, pressure, and kinetic energy all compare favorably with the LHS62 solution in both phase and magnitude. Under the region of highest waves ($\Theta_{LW} = 90°$), where wave kinetic energy is maximal, there is a negative horizontal velocity and negative pressure anomaly. The pressure, kinetic energy, and velocity all decay in the vertical in a manner consistent with the model, but the observations decay somewhat more rapidly with depth, suggesting that Δk may be slightly overpredicted. The magnitude of the vertical velocity agrees reasonably well with the LHS62 theory, but there is a subtle phase shift with the maximum upward velocity leading the theory by ~20°, on average. This phase shift is slightly less at the two lowermost ADVs, but it still leads the theory by ~10°.

The much shorter deployment of the horizontal-oriented ADCPs can be analyzed in the same way to resolve the horizontal structure of the group-bound long wave. The group phase is defined at the tower, and the two orthogonally oriented ADCPs resolve the phase-averaged along-beam velocity out to a range of 30 m (Fig. 7). Additionally, the wave band variability of along-beam velocity at each horizontal location can be used to estimate the group envelope replacing η in Eq. (12). Over this shorter deployment, the mean wave direction was from 230°N, which is more aligned with the beam of 16-Hz ADCP but directed toward both ADCPs (Fig. 1 inset). The sign of the phase-averaged along-beam velocity for both ADCPs is consistent with a group-bound long wave with positive velocity (e.g., toward the ADCP) under the low waves and negative velocity under the high waves. The horizontal velocity and the estimate of the group envelope are coherent out to >30 m in both directions, consistent with the estimates of the group wavelength, which are 50–80 m during this period [from Eq. (14)]. The slope of the velocity and wave envelope contours and their magnitude indicate wave groups that are propagating nearly parallel and perpendicular to the 16- and 8-Hz ADCPs, respectively.

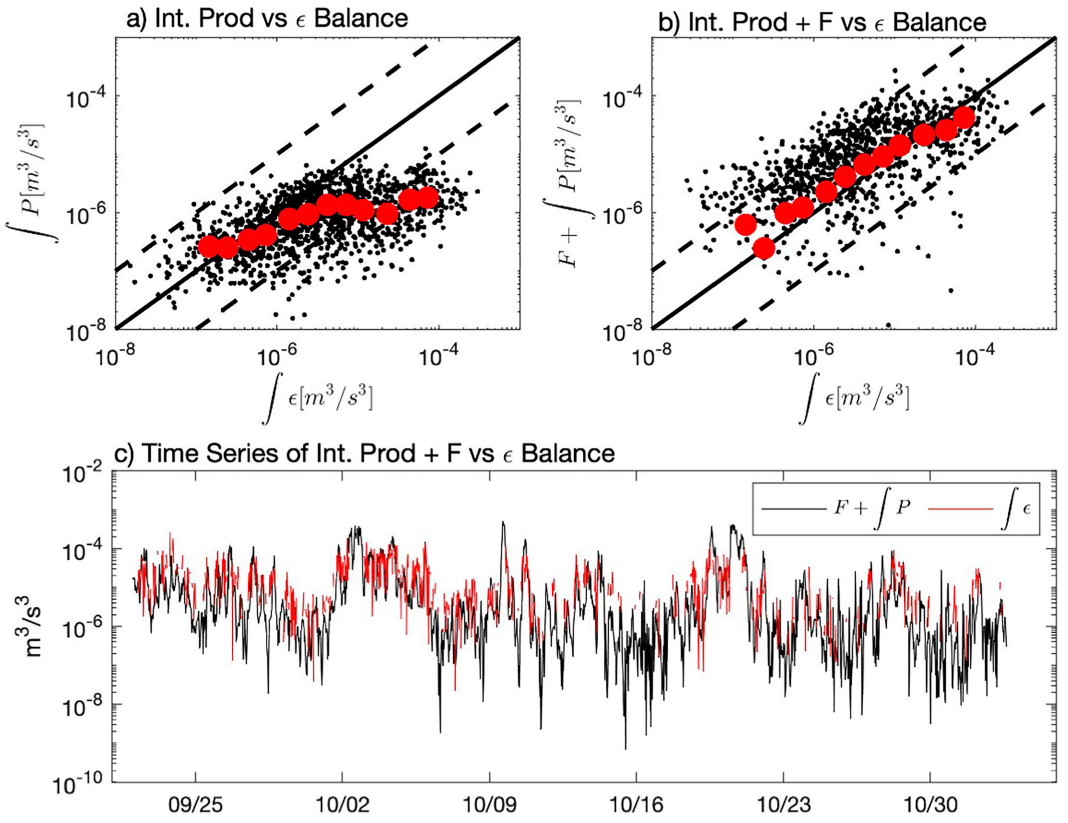

FIG. 4. Estimates of the vertically integrated TKE balance including (a) a scatterplot of the integrated dissipation and integrated shear production, (b) a scatterplot of the integrated dissipation and the sum of the integrated shear production and the downward energy flux measured at the uppermost ADV ($z \sim -1.8$ m), and (c) a time series of the same data depicted in (b). Consistent with Fig. 3, the dominant balance under energetic conditions is between the integrated dissipation and the downward flux of energy measured at $z \sim -1.8$ m.

To better highlight the temporal variability, phase-averaged contours of velocity and pressure observed at the uppermost ADV for the entire fall deployment are compared to theory in Fig. 8. There are clear increases in group-bound long-wave energy during conditions of strong surface wind forcing, and the observations and theory exhibit consistent temporal variability. The magnitude and phase of the horizontal velocity and pressure are highly consistent, but the consistent phase shift in the observed vertical velocity relative to theory is clear when plotted in this manner. The greatest phase shifts tend to occur during conditions when there is strong wind and wave forcing. An important consequence of this phase shift is that vertical velocity and pressure are no longer 90° out of phase, resulting in negative covariance between vertical velocity and pressure (e.g., downward energy flux via pressure work). To highlight the importance of this phase shift, the data are compared for condition when there is strong and weak covariance between the phase-averaged observed vertical velocity and pressure (Fig. 9). Here, "strong" and "weak" are defined simply based on the median value of the phase-averaged p–w covariance, which is nearly always negative. The observed horizontal velocity and pressure have essentially the same phase relationship for conditions with both strong and weak pressure work. However, there is a dramatic phase shift in the vertical velocity from ~0° for weak pressure work to ~40° for strong pressure work.

The clear phase shift seen in Fig. 9 suggests that an additional physical process not included in the LHS62 theory contributes to the observed vertical velocity. The consistency of this phase shift, and the persistence of negative pressure work, indicates that the process driving this additional vertical velocity has a relatively fixed relationship to the observed wave groups. To better visualize this additional circulation, the mean difference between the observed and theoretical velocity is plotted in Fig. 10a. This residual circulation is generally upward under the large wave groups and downward under the small wave groups, but the maximum upward/downward residual velocity is shifted slightly forward (relative to direction of long-wave propagation) from the maximum/minimum of the group wave envelope. It is important to note that unlike the LHS62 solution, the observed circulation does not satisfy continuity in two dimensions (x and z). The vertical ADV array provides reasonably direct estimates of $\partial w/\partial z$, and the horizontal convergence of the group-bound long wave can be estimated as $\partial u/\partial x \sim \partial u/\partial t C_g^{-1}$. With these estimates, we calculate the residual convergence/divergence, which is displayed

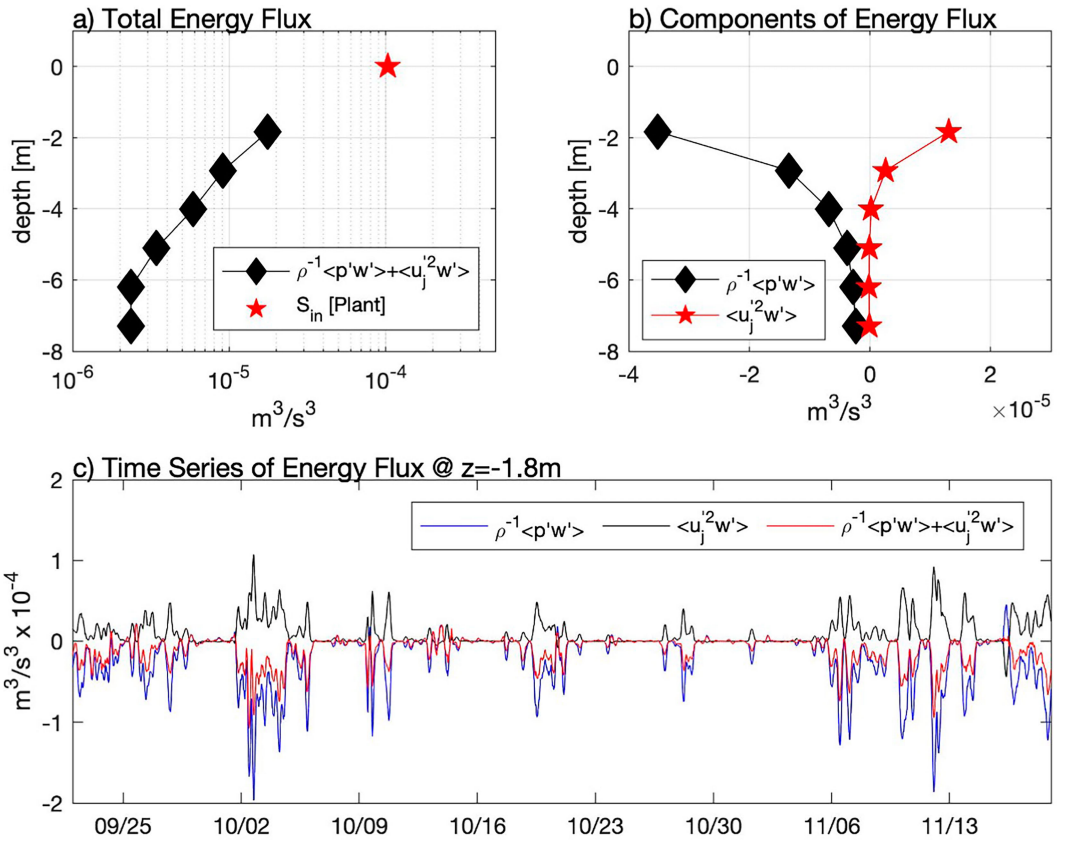

FIG. 5. (a) Profiles of the average vertical energy flux (including both pressure work and TKE transport), which is directed downward (negative) at all locations; (b) profiles comparing the pressure work (black diamonds) and TKE transport (red stars); and (c) time series of the pressure work (blue line), TKE transport (black line), and total vertical energy flux (red line) for the entire fall 2022 experiment. In (a), the red star is the surface wind input S_{in} estimated following Plant (1982). The data in (a) and (b) are averaged over all conditions where the wind speed is greater than 8 m s^{-1}. Consistent with Scully et al. (2016), the TKE transport is upward (positive) and the pressure work is negative (downward) and larger in magnitude, so that the total energy flux is downward.

in Fig. 10b. This residual is suggestive of an additional process that is convergent under the high waves (where the upward velocity is divergent) and divergent under the low waves (where the downward velocity is convergent). The inferred convergence/divergence is maximal at a depth of 4–5 m and approaches zero closer to the surface. We assume the sign of the inferred convergence/divergence changes near the surface, with near-surface convergence under the low waves driving the observed downwelling and near-surface divergence under the high waves to accommodate the observed upwelling. However, the measurements are not close enough to the surface to resolve this region.

d. *Langmuir circulation*

The classic picture of LC is two counterrotating vortices, and the associated surface convergence drives strong downwelling. The inferred residual convergence/divergence seen in Fig. 10b is consistent with the lower half of this picture, but the near-surface region is not resolved. The upward-looking ADCP provides a more complete view of the water column, and during conditions with strong wind forcing, features that are broadly consistent with LC are ubiquitous. The high-resolution echo intensity data demonstrate coherent regions of high backscatter that extend from the surface to depths of ~8 m (Fig. 11a). These regions of high backscatter are often associated with low-frequency (<1/15 Hz) downward vertical velocities of ~0.05 m s^{-1} that persist for several minutes (Fig. 11b). We interpret these features as plumes of small bubbles created by wave breaking at the surface that are advected downward by relatively strong and coherent vertical motions. These strong low-frequency downward velocities often coincide with strong downwind horizontal velocity anomalies, generally consistent with the assumed structure of Langmuir circulation.

While the upward-looking ADCP resolved these vertical structures, the two orthogonally oriented ADCPs provide a more complete view of the horizontal variability near the surface ($z \sim -3.5$ m). The 5th beam of the 16-Hz ADCP, which was oriented toward ~220°, recorded alternating bands of high and low backscatter that were largely coherent over most of the sampling array (~30 m) (Fig. 11c). The acoustic backscatter is significantly ($p < 0.01$) correlated ($r = 0.48$)

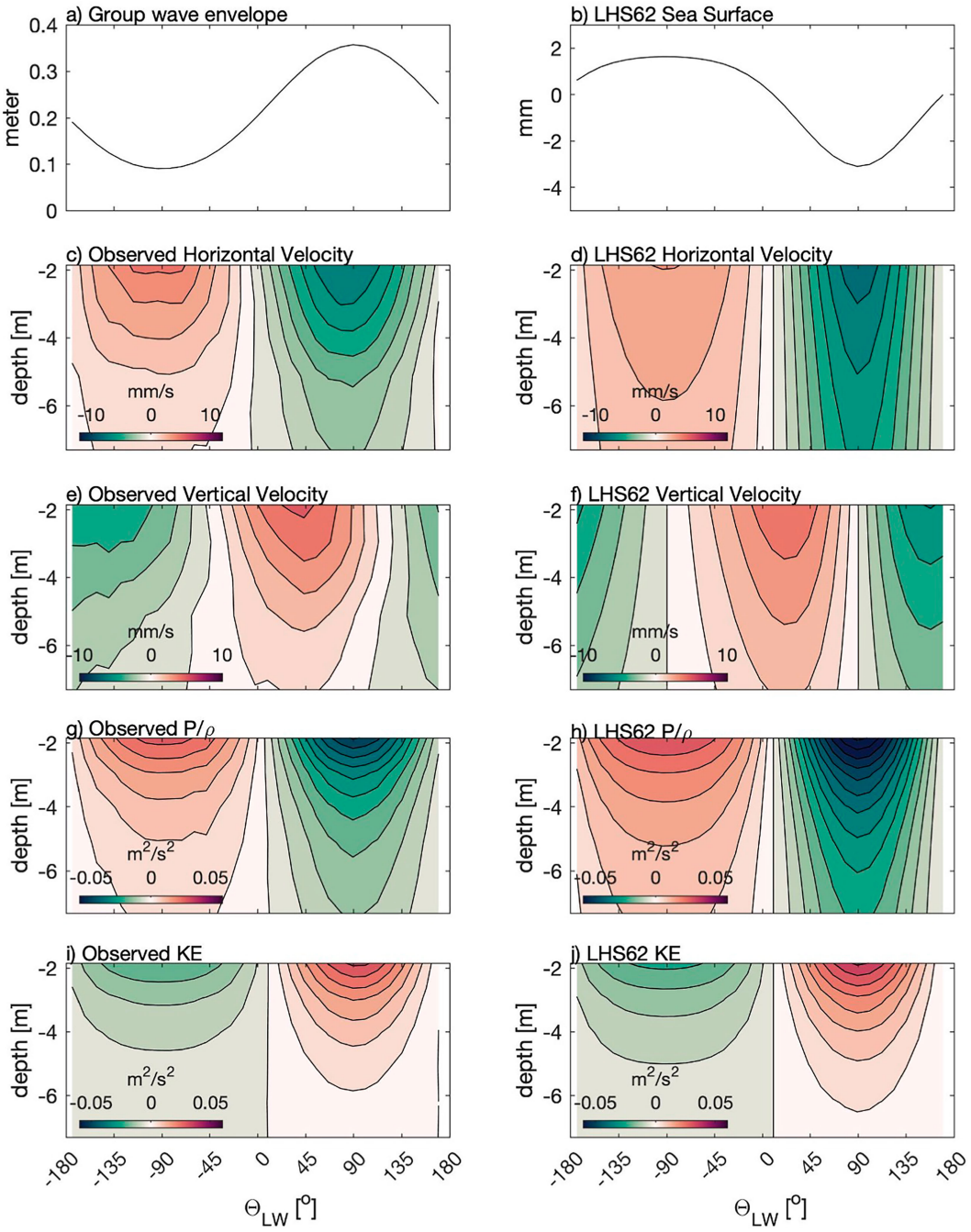

FIG. 6. Observations of group-bound long-waves compared to the theory of Longuet-Higgins and Stewart (1962). All data have been averaged as a function of the group-bound long-wave phase [Eq. (13)] and averaged over all conditions where the wind speed is greater than 8 m s^{-1}. Data include (a) observed group wave envelope, (b) predicted sea surface elevation, (c) observed horizontal velocity, (d) predicted horizontal velocity, (e) observed vertical velocity, (f) predicted vertical velocity, (g) observed pressure, (h) predicted pressure, (i) observed kinetic energy, and (j) predicted kinetic energy.

with the along-beam velocity, with regions of high backscatter generally associated with positive along-beam velocities (toward the sensor) and low backscatter associated with negative along-beam velocities (away from the sensor) (Fig. 11d). During this period, the tidal current was ebbing (directed toward ~230°N) and the high/low backscatter regions appeared first at the bins closest to the sensor and were advected away from the sensor consistent with bubble streaks that were

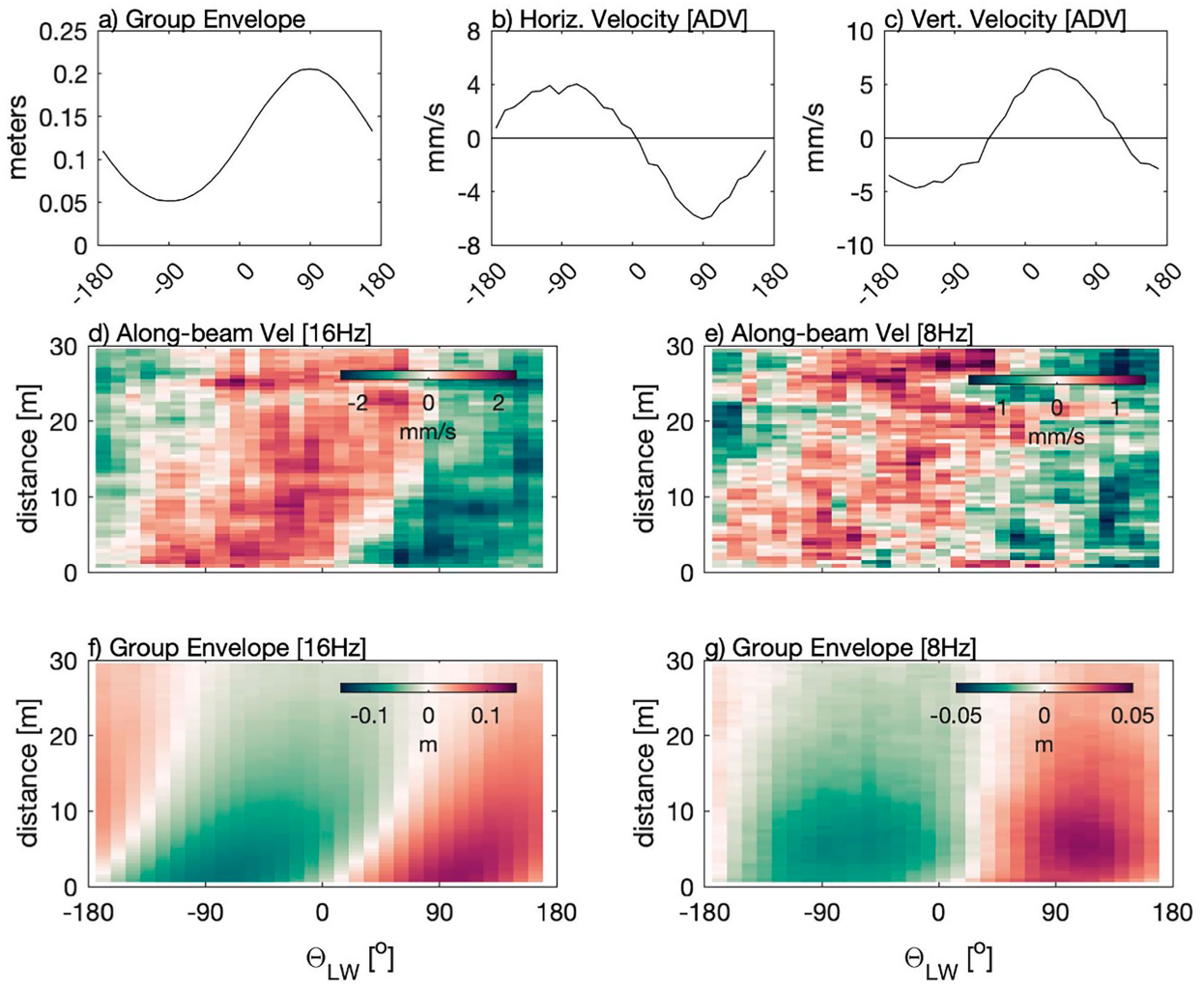

FIG. 7. Observations of the horizontal structure of group-bound long waves resolved by the horizontal-looking ADCPs ($z \sim -3$ m) during the 11–12 Nov 2022 deployment. All data have been averaged as a function of the group-bound long-wave phase [Eq. (13)] defined using the pressure observed at the tower and averaged over conditions where the wind speed is greater than 8 m s^{-1} (~18 h). Data include (a) observed group wave envelope at the tower, (b) horizontal velocity measured by the uppermost ADV, (c) vertical velocity measured by the uppermost ADV, (d) along-beam velocity measured by the 16-Hz ADCP, (e) along-beam velocity measured by the 8-Hz ADCP, (f) estimate of the group wave envelope from the 16-Hz ADCP, and (g) estimate of the group wave envelope from the 8-Hz ADCP. Estimates of the group wave envelop for the horizontal-looking ADCPs in (f) and (g) are obtained via Eq. (13) using the wave band fluctuations of the along-beam velocity at a proxy for sea surface elevation. For both ADCPs, positive along-beam velocity is defined as toward the ADCP, consistent with group-bound long waves propagating from the S/SW to the north (N)/NE. Both the along-beam velocity and group envelope are coherent to ~30 m when averaged this way.

roughly oriented parallel to the wind, which was blowing from ~180°N. Six hours later during the flooding phase of the tide, the opposite pattern was observed with the streaks advecting toward the sensor (not shown). The bottom-mounted upward-looking ADCP is located roughly 20 m from the tower, and the near-surface backscatter observed by this instrument is highly correlated with backscatter observed by the 16-Hz ADCP at a range of 20 m, suggesting that these instruments are sampling the same features.

At the 8-Hz ADCP, which was oriented toward ~310°N, similar bands of high and low backscatter were observed, and the low-frequency along-beam velocity was negatively correlated with the acoustic backscatter anomaly. This negative correlation is consistent with our assumption that a downwind LC velocity anomaly would show up as a negative along-beam velocity (away from the sensor) at the 8-Hz ADCP (e.g., Fig. 1b). The negative correlation between backscatter anomaly and low-frequency along-beam velocity at this location is weaker in magnitude than the positive correlation observed at the 16-Hz ADCP, presumably because the downwind velocity anomaly is much better aligned with the 16-Hz beam.

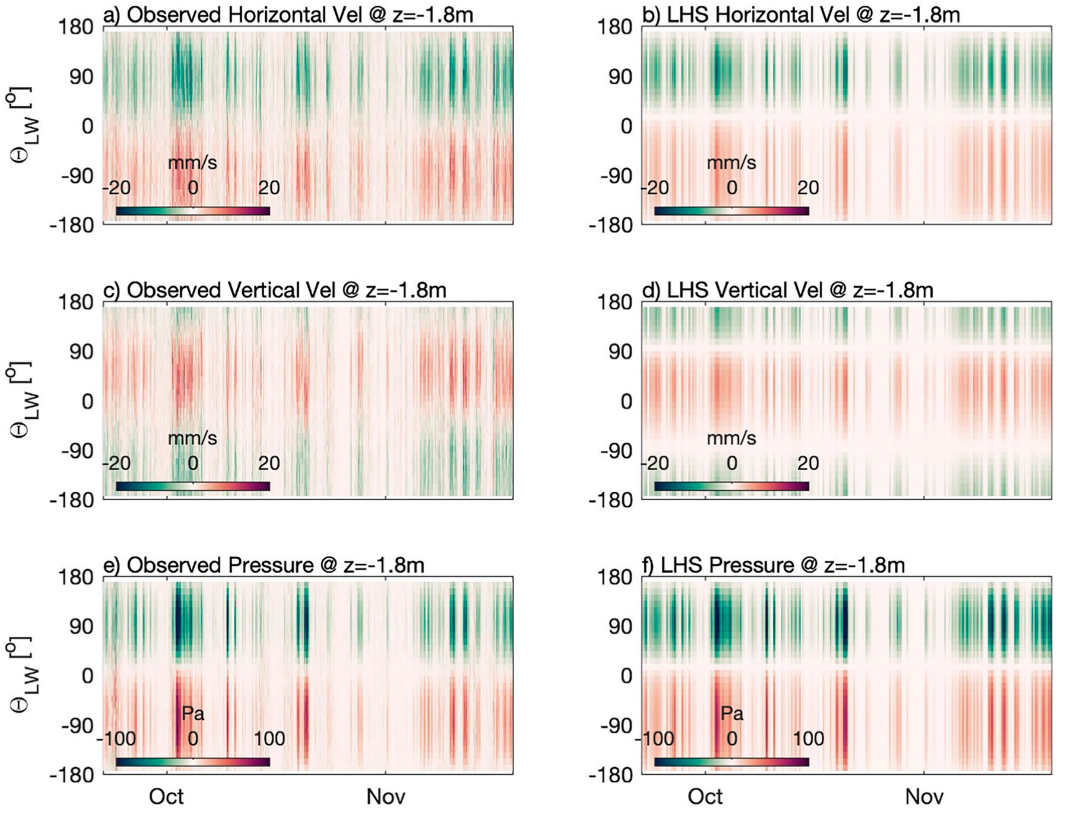

FIG. 8. Time series of the observed and predicted (LHS62) phase-averaged (a),(b) horizontal velocity; (c),(d) vertical velocity; and (e),(f) pressure for the entire fall 2022 experiment. Data are from the uppermost ADV ($z \sim -1.8$ m) and are averaged as a function of the group-bound long-wave phase [Eq. (13)] for each 20-min burst. When plotted this way, the observations compare favorably to the LHS62 solution, except for the phase shift between the observed and predicted vertical velocities, which is more apparent during strong wind/wave forcing.

Simple estimates of the width of the streaks are obtained from the along-beam backscatter measurements. For each ping, the width of the high backscatter region is calculated from the up- and downcrossing of the along-beam backscatter anomaly. For the burst shown in Fig. 11, the width of the high backscatter region is ~7.8 and ~7 m for the 16- and 8-Hz ADCPs, respectively. This is consistent with streaks that have a −42° orientation relative to the 16-Hz ADCP beam, which

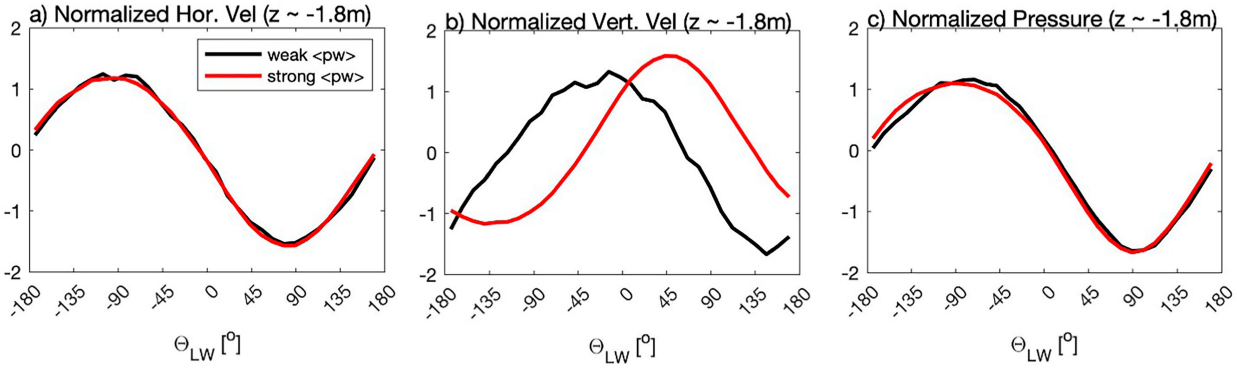

FIG. 9. Phase-averaged and normalized observations from the uppermost ADV ($z \sim -1.8$ m) of (a) horizontal velocity, (b) vertical velocity, and (c) pressure for conditions with strong downward energy flux (red line) and weak downward energy flux (black line). On all plots, the phase-averaged data are normalized by their standard deviation to highlight changes in phase. Strong and weak energy flux is defined based on the upper and lower quartiles of the observed pressure work. Strong downward energy flux appears to be driven primarily by a significant positive phase shift in the vertical velocity relative to the expect relationship from the LHS62 solution.

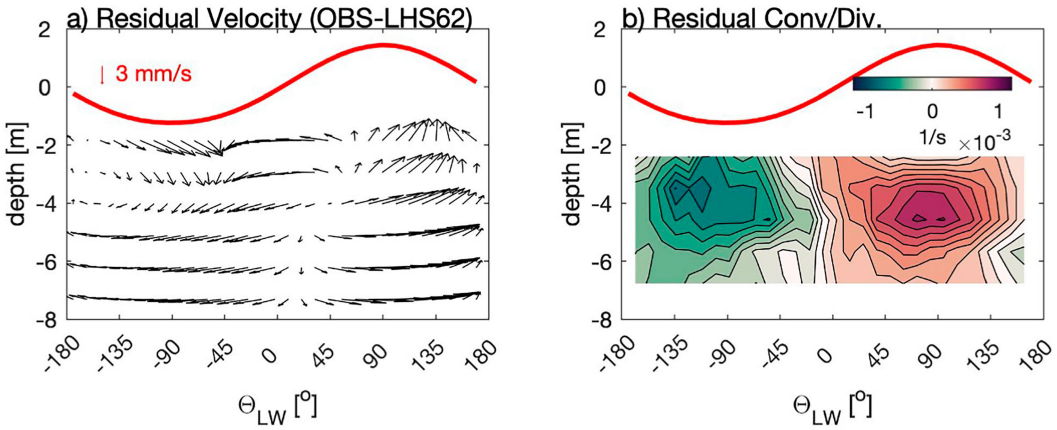

FIG. 10. Phase-averaged (a) residual velocity and (b) convergence/divergence for conditions when the mean wind speed is greater than 8 m s^{-1}. The residual velocity is simply the difference between the observed velocity and the LHS62 solution (observed minus prediction). Unlike LHS62, which satisfies continuity, the observed phase-average circulation does not, implying that there is an additional process that must drive the observed convergence/divergence depicted in (b). In both (a) and (b), the red line indicates the group-wave envelope (not to scale). Under the high groups of waves, the residual circulation is upward and divergent, suggesting there must be additional convergence to satisfy continuity. Conversely, the residual circulation is downward and convergent under the low waves, implying an additional process that is divergent over the resolved portion of the water column. Note that these measurements do not resolve the near-surface layer, where we assume the sign of the convergence/divergence must change to drive the observed residual vertical velocity.

translates into an orientation of 178°–358°N—close to the wind direction at this time. Based on these geometric arguments, the transverse width of the high backscatter region is 5.2 m giving a streak spacing of 10.4 m, which is similar to the depth of penetration observed in the upward-looking ADCP.

It is instructive to examine one specific event in more detail to gain insight into the overall structure of these features and to help interpret the data collected by the ADVs. Figure 12 shows the echo sounder data from the upward-looking ADCP for the high backscatter/strong downwelling event observed in Figs. 11a and 11b between 0203:50 and 0206:30 LT. Superimposed on the echo sounder data are the vectors of low-frequency (<1/15 Hz) vertical and across-wind velocities measured by the ADCP. The downward jet extends nearly all the way to the bottom, generally coincident with the elevated echo intensity. These data are collected at a fixed location, but we assume that they capture the spatial variability as the current advects the slowly evolving circulation structure past the ADCP. The intensity of the downwelling jet decreases with depth, suggesting vertical convergence, and the lateral (across-wind) velocity is divergent over most of the resolved portion of the water column, consistent with Fig. 10. Side-lobe interference prevents resolving the velocity for $z > -2$ m, but there are hints that this strong downwelling is driven by near-surface convergence. With this assumed convergence, the overall structure is consistent with two counterrotating vortices typically associated with LC. It is important to note that neither the upper ADV nor the ADCP fully resolves this near-surface convergence, which must occur to support such strong downwelling (~0.05 m s^{-1}).

This is just one example, and it is useful to synthesize more data to provide a more representative analysis. To that end, we average all the horizontal ADCP data collected over conditions when the wind speed exceeded 8 m s^{-1}. This covers the main storm event on 11–12 November, that lasted roughly 18 h. During this storm, the winds were primarily from the south (S), rotating from southeast (SE) to SW with maximum winds peaking at 14 m s^{-1}. We employ a phase averaging like that used above, but here, we seek to isolate the signal associated with the LC. Therefore, we define the phase based on the real and imaginary parts of the Hilbert transform of the low-frequency vertical velocity ($\Theta_{LC} = \tan^{-1}[\text{real}\{H\{\text{wlow}\}\}, \text{imag}\{H\{\text{wlow}\}\}]$) measured by the uppermost ADV. Using this definition of phase, the maximum downward and upward velocities occur at $\Theta_{LC} = -90°$ and $\Theta_{LC} = 90°$, respectively. When averaged this way, the vertical and horizontal (rotated into the wind direction) velocities are nearly −180° out of phase, consistent with a downward flux of horizontal momentum (Figs. 13a,b). At the 16-Hz ADCP, the along beam velocity at the bins closest to the sensor (and ADVs) is positive (toward the ADCP) for downward vertical velocity and negative for upward vertical velocities, consistent with the ADV data (Fig. 13c). The along-beam velocity is coherent out to >15 m but is angled in phase space consistent with streaks that are angled relative to the beam orientation. This angle is consistent with streaks that are generally aligned with the wind, which is blowing from a lesser angle than the beam orientation throughout the storm. The positive/negative velocity anomalies are positively correlated with high/low acoustic backscatter consistent with the high backscatter occurring in the downwind/downwelling jets (Fig. 13d). In the 8-Hz ADCP, the along-beam velocity is negative during downwelling and positive during upwelling for the bins closest to the sensor (Fig. 13e). The sign of the along-beam velocity is

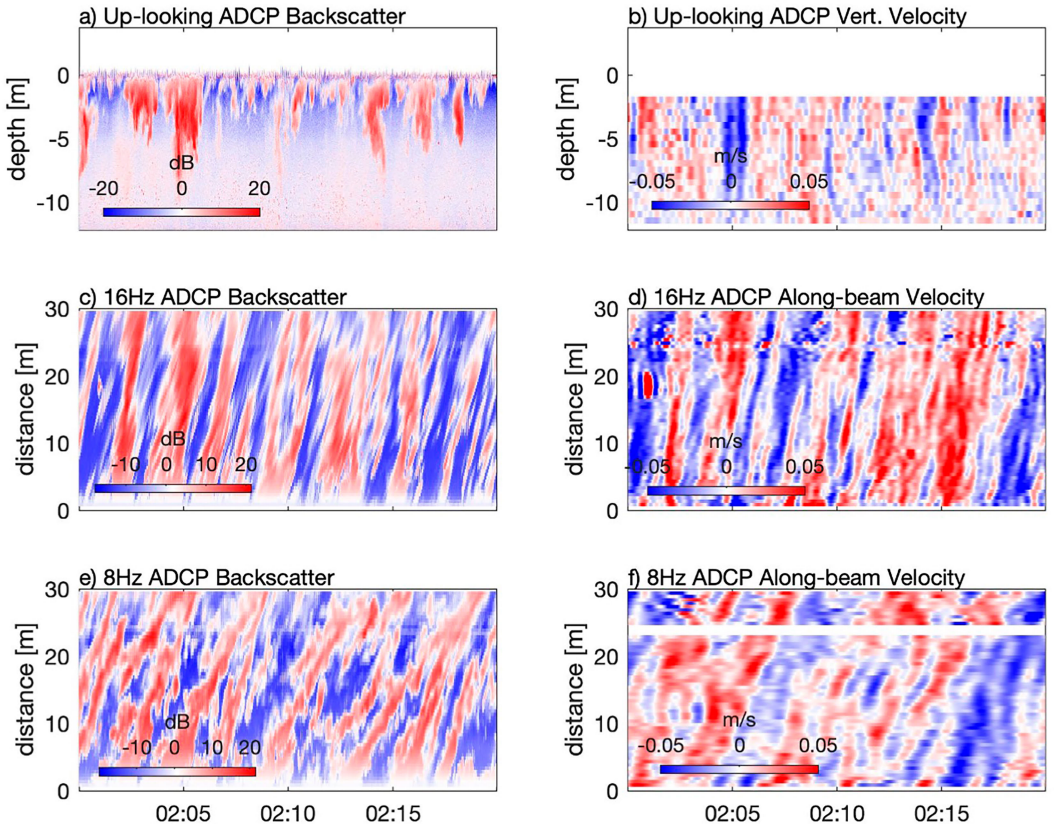

FIG. 11. Examples of LCs from the upward- and horizontal-looking ADCPs on 12 Nov 2022, including (a) acoustic backscatter from upward-looking ADCP; (b) vertical velocity from upward-looking ADCP; (c) acoustic backscatter from horizontal-looking 16-Hz ADCP; (d) along-beam velocity from horizontal-looking 16-Hz ADCP; (e) acoustic backscatter from horizontal-looking 8-Hz ADCP; and (f) along-beam velocity from horizontal-looking 8-Hz ADCP. The velocity data have all been low-pass filtered to remove variability at frequencies greater than 1/20 Hz.

consistent with LC streaks that are aligned with the wind, which would be away from the sensor (negative) during this storm event. The sign of the along-beam velocity changes quickly moving away from the tower along the 8-Hz beam, consistent with a streak that is ~6 m wide and aligned roughly with the wind. At the 8-Hz location, the along-beam velocity and acoustic backscatter are negatively correlated.

These measurements from ADCPs indicate that LC is a consistent feature during energetic wind conditions. They exhibit horizontal and vertical motions that are coherent at length scales similar to the water depth, and the along-wind horizontal velocity is ~180° out of phase with the vertical velocity, suggesting that these motions contribute significantly to the vertical momentum flux. We estimate the momentum flux crudely from the upward-looking ADCP data as

$$\overline{u'w'} \approx \overline{\widetilde{u_{\mathrm{adcp}}}\,\widetilde{w_5}}, \tag{15}$$

where the tilde indicates that both the horizontal u_{adcp} and vertical fifth beam w_5 ADCP velocities have been demeaned and low-pass filtered to remove motions at frequencies above 1/15 Hz. Additionally, u_{adcp} is rotated into the direction of the mean wind. During conditions with energetic winds, the ~180° phase difference between the low-frequency horizontal and vertical motions results in significant downward flux of horizontal momentum (Fig. 14). The momentum flux penetrates to depths approaching 10 m, consistent with the coherent vertical motions that we attribute to LC (e.g., Figs. 11a,b). It is important to note that the horizontal velocity is calculated from the slanted ADCP beams, which have a horizontal separation of ~11 m near the surface, so the motions that are contributing to these velocity estimates must be coherent at comparable scales. This is consistent with the horizontal ADCP data that show coherence at scales approaching 20 m or greater. The ADCP estimates of momentum flux at $z \sim -3$ m are strongly correlated with directly measured surface stress from the lowest sonic anemometer on the tower, but the ADCP estimates are approximately 50% smaller.

6. Discussion and conclusions

In the data presented above, we document that elevated dissipation in the WASL results from the vertical convergence in energy flux driven by pressure work (Fig. 3). While consistent with a balance between transport convergence and dissipation suggested in previous work (Craig and Banner 1994;

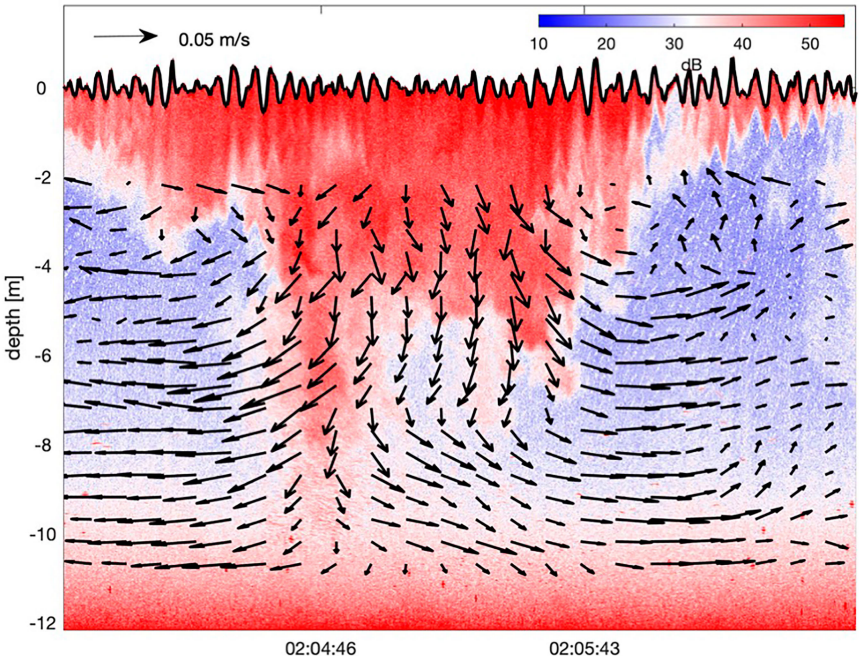

FIG. 12. Detail of the strong downwelling—high backscatter event observed by the upward-looking ADCP at 0203:50–0206:40 LT 12 Nov 2022. Color contours are the high-resolution (~1.2 cm) echo intensity data from the upward-looking ADCP and the arrows depict the observed low-frequency (<1/15 Hz) vertical and across-wind velocities. Consistent with Fig. 10b, the downwelling jet is convergent driving a divergent flow at depth. There is some evidence for near-surface convergence, but the velocity in the near-surface region is not well-resolved due to side-lobe interference. However, the overall structure of the downwelling jet is largely consistent with two counterrotating vortices.

Terray et al. 1996), it is inconsistent with the idea that this transport is due to enhanced near-surface TKE that is carried downward by larger eddies, which would be expected to result in downward kinetic energy flux. In contrast, the kinetic energy flux is upward, and the pressure work is downward (Fig. 5b). We explored the hypothesis that the pressure work in the WASL is driven by an interaction between LC and wave groups, where downward vertical velocity under low groups of waves and upward vertical velocity under high groups of waves drive the downward flux energy. The horizontal velocity, pressure, and kinetic energy we observe compare favorably with group-bound long-wave theory (Figs. 6 and 8), but the vertical velocity exhibits a positive phase shift during energetic conditions (Fig. 9), which results in the observed downward energy flux driven by pressure work. We also document energetic LC that drives strong downward vertical velocities in association with positive downwind velocity, resulting in appreciable vertical momentum flux (Figs. 12–14). Our primary hypothesis is that the phase shift in the observed vertical velocity relative to the group wave is the result of weak coupling between the LC and the wave groups. The CL1 mechanism, where horizontal gradients in the Stokes drift drive the Langmuir instability, provides such a link and is consistent with the observed downwelling centered on the groups of low waves (e.g., Fig. 10a).

Consistent with the recent simulations of Fujiwara and Yoshikawa (2020), we hypothesize that the importance of the CL1 mechanism in this dataset is the result of wave–current interaction, a process ignored by nearly all other numerical simulations. Our results suggest that this interaction is relatively weak, and the basic patterns we observe are only revealed through extensive averaging. The vertical velocity anomalies associated with what we interpret as LC are ~0.03 m s^{-1} (e.g., Figs. 11a and 12), much stronger than the inferred average residual circulation ~0.003 m s^{-1} (e.g., Fig. 10a). Thus, we hypothesize that wave–current interaction slightly modifies the wave group structure but does not fundamentally set the across-wind length scale of the wave groups. We infer LC streaks that have a spacing of ~10 m, whereas the wave groups have lengths on the order of ~60 m, or greater. The horizontal ADCPs demonstrate that the wave groups are coherent at scales > 30 m in both the along and across-wave direction (Fig. 7), in contrast to the <10 m across-wind variability associated with LC (Fig. 13). Nonetheless, the strong vertical velocities associated with the LC combined with large pressure anomalies associated with the wave groups result in appreciable energy flux, despite the weak coupling.

The mismatch we observe in spatial scales is consistent with the clear frequency separation we observe between the momentum flux and energy fluxes. Figure 15 compares the variance-preserving cospectrum and magnitude-squared coherence (MSC)

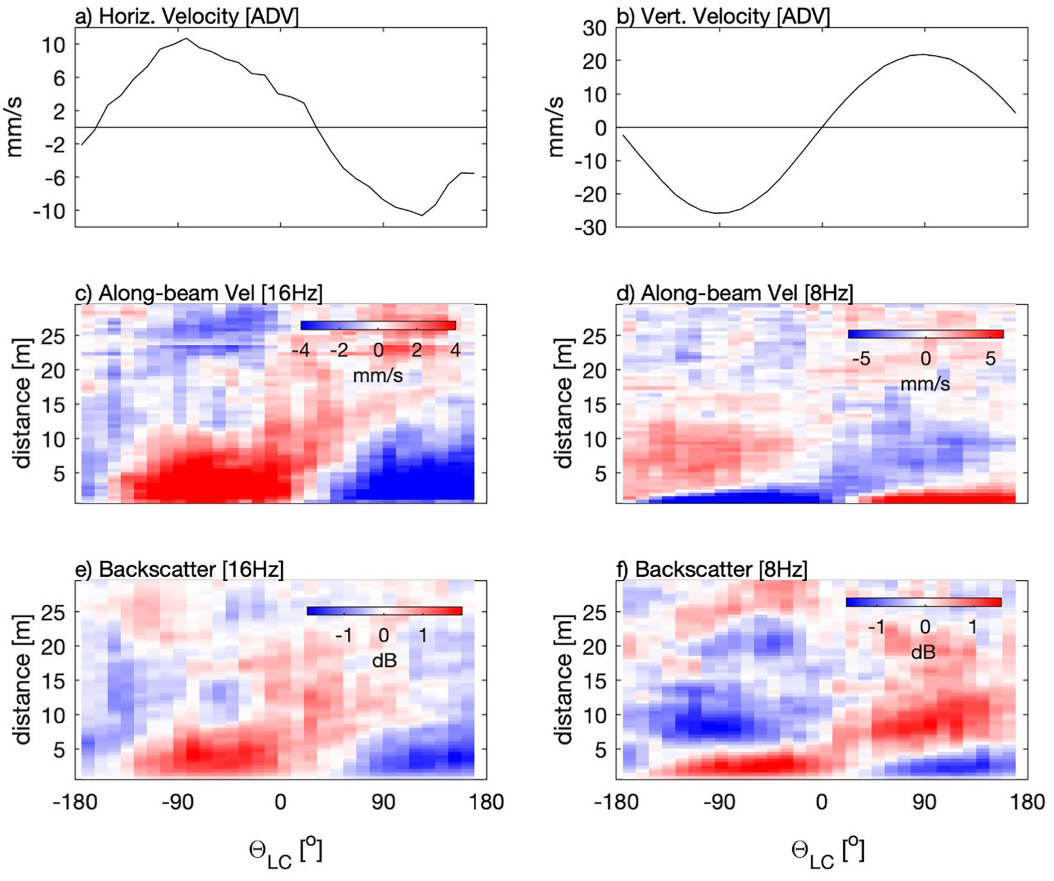

FIG. 13. Phase-averaged data from the horizontal-looking ADCPs, where the phase is now defined based on the low-frequency vertical velocity (e.g., Θ_{LC}) to better isolate motions associated with LC. Data include (a) horizontal velocity from the uppermost ADV, (b) vertical velocity from the uppermost ADV (which defines the phase), (c) along-beam velocity from the 16-Hz ADCP, (d) along-beam velocity from the 8-Hz ADCP, (e) acoustic backscatter from the 16-Hz ADCP, and (f) acoustic backscatter from the 8-Hz ADCP. Acoustic backscatter and along-beam velocity are positively correlated at 16 Hz and negatively correlated at 8 Hz, consistent with high backscatter in downwind jets directed toward the 16-Hz ADCP and away from 8 Hz (e.g., roughly aligned with the wind). Unlike the group-bound long-wave structure (e.g., Fig. 7), the structure attributed to LC is coherent over much shorter length scales (<10 m).

of the momentum flux and energy fluxes. Presumably, the cospectra and MSC would have similar frequency distribution if the same physical process driving the momentum flux was also driving the energy flux. However, the variance-preserving cospectrum and MSC for momentum peak at much lower frequency (~1/180 Hz) than the vertical energy fluxes (both pressure and TKE), which are maximal at ~1/20 Hz. These data indicate a clear frequency separation between the downward flux of momentum and the vertical fluxes of energy. We assume that the momentum cospectra include the energetic LC, which advect past the fixed sensors with the mean currents (~0.10 m s^{-1}). This advection speed U suggests a length scale $L \sim U$/freq of ~20 m, generally consistent with the measured scales of LC. A similar argument would suggest that the length scale of energy flux is much smaller (~2 m). However, the dominant pressure and energy anomalies we observe travel at the group velocity (C_g ~3 m s^{-1}), which we argue is the appropriate advective speed (e.g., $L \sim C_g$/freq). This would indicate that the length scale of energy flux is ~60 m, which is the mean wavelength of the observed wave groups.

Given these arguments, we hypothesize that LC plays a key role in the vertical transport of momentum, and that the vertical flux of energy in the WASL occurs as wave groups propagate through, and only weakly interact with, LC. The statistical relationship between downward/upward vertical velocity of the LC and high/low pressure of the group wave is consistent with the CL1 mechanism and is hypothesized to be the result of wave–current interaction. To look for evidence of this interaction, we use the uppermost collocated velocity and pressure measurements to define an instantaneous wave direction. The 32-Hz ADV data are rotated into a coordinate system based on the direction of the dominant surface waves, and these data are used to define the instantaneous wave direction:

$$\theta_w = \tan^{-1}(\tilde{v}\tilde{p}, \tilde{u}\tilde{p}), \tag{16}$$

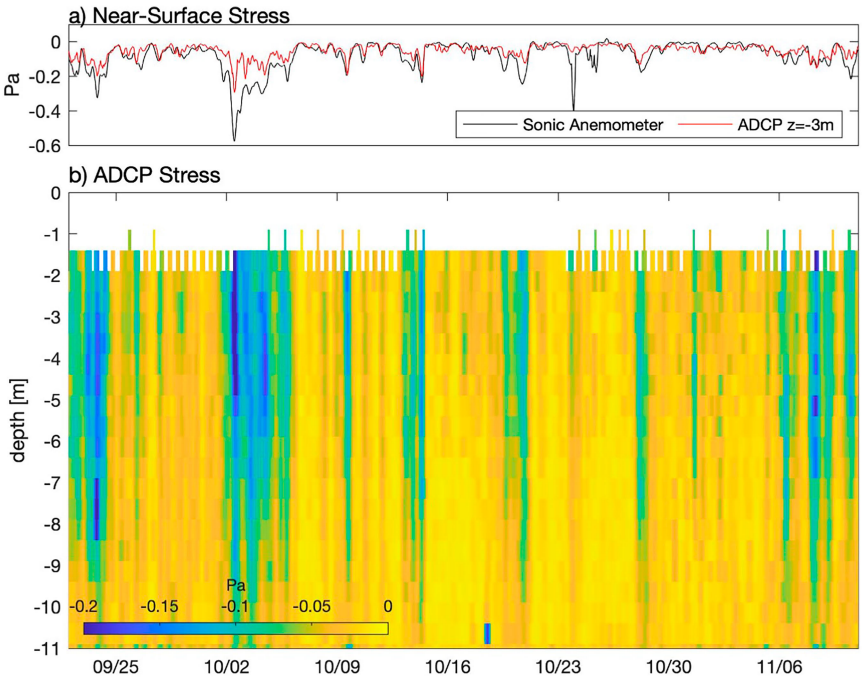

FIG. 14. Crude estimates of momentum flux calculated from the upward-looking ADCP. (a) The near-surface ADCP estimate is compared to the surface momentum flux from the lower-most sonic anemometer. (b) Full water column contours of momentum flux are presented. ADCP estimates are simply the product of the low-pass filtered (<1/15 Hz) along-wind and vertical velocities to highlight that the physical process driving the momentum flux has spatial scales that are coherent at spatial scales up to, and exceeding, the horizontal beam separation, which is >10 m near the surface.

where the tilde indicates that the data have been bandpass filtered (1/10 < freq < 1 Hz) to isolate the dominant wave motions. Directional histograms $[D(\theta_w)]$ are compared for conditions when the demeaned and low-pass-filtered (freq < 1/15 Hz) current at the uppermost ADV is directed with $[D(\theta_w)_{\text{pos}}]$ and against $[D(\theta_w)_{\text{neg}}]$ the direction of wave propagation. To highlight the differences caused by local currents, positive and negative anomalies are defined by the upper and lower quartiles of

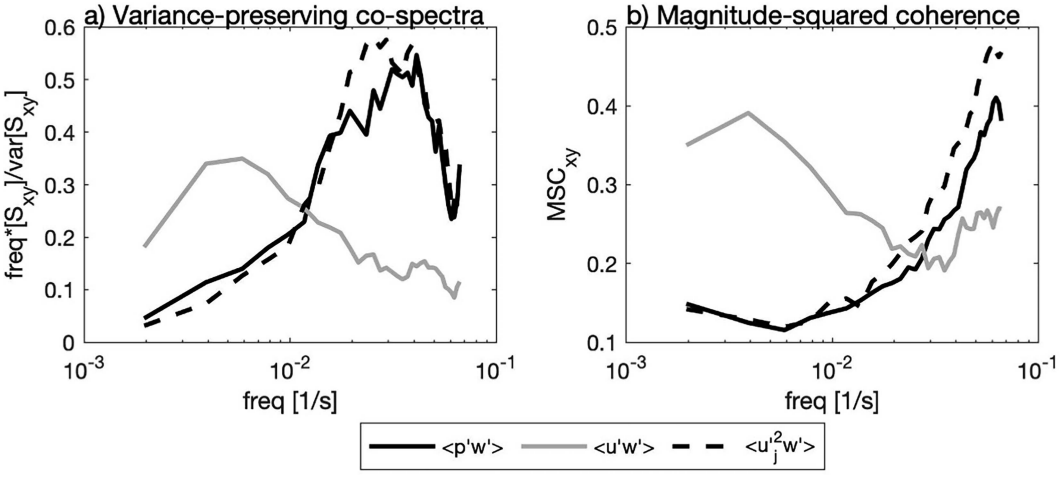

FIG. 15. (a) Variance-preserving cospectrum and (b) MSC of pressure–vertical velocity (solid black line); kinetic energy–vertical velocity (dashed black line); and horizontal velocity–vertical velocity (solid gray line). Both the cospectrum and MSC have been averaged over all conditions where wind speed exceeds 8 m s^{-1}. The variance-preserving cospectrum also has been normalized by the total covariance so that the area under each curve is the same. Note that in frequency space, there appears to be a large separation between the momentum flux and the energy flux.

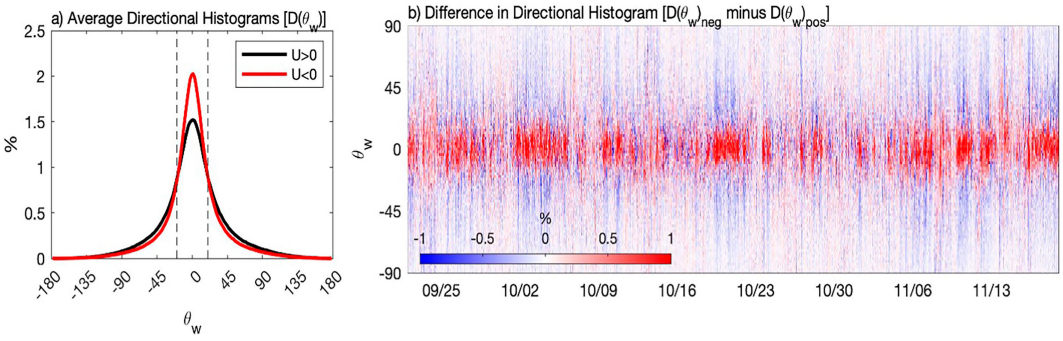

FIG. 16. Histograms of the instantaneous wave direction from the upper-most ADV ($z \sim -1.8$ m). (a) Comparison of the averaged histograms when the velocity anomaly attributed to LC is in the same direction as the waves (black line) to conditions when the velocity anomaly is opposite the waves (red line). The velocity anomaly is defined based on the low-pass-filtered (<1/15 Hz) and detrended along-wind velocity measured at the uppermost ADV for each burst. (b) Contours of the difference between the histograms for negative and positive velocity anomalies $[D(\theta)_{\text{neg}} - D(\theta)_{\text{pos}}]$ to show the consistent behavior throughout the experiment. In (a), the dashed vertical lines correspond to $\theta_w = \pm 20°$, highlighting that there is roughly 20% more wave energy directed downwind when the near-surface velocity anomaly is negative (e.g., opposing the direction of wave propagation).

the low-pass-filtered along-wave velocity for each burst. As seen in Fig. 16, when the low-frequency current (presumed to be LC) is directed with the waves, there is greater directional spreading than observed for periods when the current is opposing wave propagation. On average, there is roughly 20% more energy directed within the range $-20° < \theta_w < 20°$ for conditions when there is a negative LC current anomaly (opposing the waves) than for conditions with a positive LC current anomaly (directed with waves). This result is consistent with wave refraction by the local current, which we assume is the result of Langmuir turbulence. This argument assumes that the current anomaly observed at the uppermost ADV represents a local maximum/minimum, and that the current magnitude decreases in the lateral (across-wave) direction, consistent with the features seen in Figs. 11d and 11f. Thus, the across-wave velocity shear associated with a positive anomaly would act to spread out wave energy, whereas the velocity shear associated with a negative anomaly would act to focus wave energy for conditions when the wind, waves, and LC are aligned. We expect wave–current interaction to occur when the spatial scales of current are comparable to the length scale of the surface waves. The wavelength of the dominant 3–4-s waves observed at this location is 15–25 m, which is comparable to the observed scales of LC.

A primary conclusion of this paper is that refracting energy away from the downwelling regions and into the upwelling regions drives the downward flux of energy in the WASL. In a statistical sense, this refraction results in lower waves, less wave kinetic energy and higher pressure in downwelling regions, and higher waves, more wave kinetic energy, and lower pressure in upwelling regions. This negative covariance between vertical velocity and pressure drives the downward energy flux via pressure work. The Bernoulli response of the sea surface results in pressure anomalies that are larger in magnitude than the associated anomalies in kinetic energy, which is why the net energy flux is downward. Additionally, the pressure anomalies extend deeper into the water column than the kinetic energy anomalies [Eq. (11)]. This downward flux of energy may represent a loss of energy from the surface wave field, which we assume is transferred to the large-scale coherent turbulence of LC. This large-scale turbulence plays a key role in the vertical momentum flux and the downward energy flux that ultimately drives enhanced dissipation in the WASL. The hypothesized importance of wave-LC interactions highlights the need for improved numerical methods to better understand the energetics of the upper ocean, including wave-resolving models that can faithfully simulate these dynamics.

Acknowledgments. We are indebted to Jay Sisson, Steve Faluotico, Oaklin Keefe, and the crew at AGM Marine for all their help in planning, deploying, and retrieving the tower and associated instruments used in this study. Funding was provided by the National Science Foundation Grant OCE-202302.

Data availability statement. Data used in this work Scully and Zippel (2023) are available through the WHOI Open Access Server (WHOAS) at https://doi.org/10.26025/1912/66837.

REFERENCES

Agrawal, Y. C., E. A. Terray, M. A. Donelan, P. A. Hwang, A. J. Williams III, W. M. Drennan, K. K. Kahma, and S. A. Krtaigorodskii, 1992: Enhanced dissipation of kinetic energy beneath surface waves. *Nature*, **359**, 219–220, https://doi.org/10.1038/359219a0.

Anis, A., and J. N. Moum, 1995: Surface wave–turbulence interactions. Scaling $\varepsilon(z)$ near the sea surface. *J. Phys. Oceanogr.*, **25**, 2025–2045, https://doi.org/10.1175/1520-0485(1995)025<2025:SWISNT>2.0.CO;2.

Arsenyev, S. A., S. V. Dobroklonsky, R. M. Maredov, and N. K. Shelkovnikov, 1975: Direct measurements of some characteristics of fine-scale turbulence from a stationary platform in the open sea. *Izv., Atmos. Ocean. Phys.*, **11**, 530–533.

Craig, P. D., and M. L. Banner, 1994: Modeling wave-enhanced turbulence in the ocean surface layer. *J. Phys. Oceanogr.*, **24**,

2546–2559, https://doi.org/10.1175/1520-0485(1994)024<2546:MWETIT>2.0.CO;2.

Csanady, G. T., 1994: Vortex pair model of Langmuir circulation. *J. Mar. Res.*, **52**, 559–581, https://doi.org/10.1357/0022240943076984.

Drennan, W. M., M. A. Donelan, E. A. Terray, and K. B. Katsaros, 1996: Oceanic turbulence dissipation measurements in SWADE. *J. Phys. Oceanogr.*, **26**, 808–815, https://doi.org/10.1175/1520-0485(1996)026<0808:OTDMIS>2.0.CO;2.

Esters, L., Ø. Breivik, S. Landwehr, A. ten Doeschate, G. Sutherland, K. H. Christensen, J.-R. Bidlot, and B. Ward, 2018: Turbulence scaling comparisons in the ocean surface boundary layer. *J. Geophys. Res. Oceans*, **123**, 2172–2191, https://doi.org/10.1002/2017JC013525.

Feddersen, F., J. H. Trowbridge, and A. J. Williams III, 2007: Vertical structure of dissipation in the nearshore. *J. Phys. Oceanogr.*, **37**, 1764–1777, https://doi.org/10.1175/JPO3098.1.

Fujiwara, Y., and Y. Yoshikawa, 2020: Mutual interaction between surface waves and Langmuir circulations observed in wave-resolving numerical simulations. *J. Phys. Oceanogr.*, **50**, 2323–2339, https://doi.org/10.1175/JPO-D-19-0288.1.

Gargett, A. E., 1989: Ocean turbulence. *Annu. Rev. Fluid Mech.*, **21**, 419–451, https://doi.org/10.1146/annurev.fl.21.010189.002223.

Garrett, C., 1976: Generation of Langmuir circulations by surface waves—A feedback mechanism. *J. Mar. Res.*, **34**, 117–130.

Gemmrich, J., 2010: Strong turbulence in the wave crest region. *J. Phys. Oceanogr.*, **40**, 583–595, https://doi.org/10.1175/2009JPO4179.1.

Gerbi, G. P., J. H. Trowbridge, E. A. Terray, A. J. Plueddemann, and T. Kukulka, 2009: Observations of turbulence in the ocean surface boundary layer: Energetics and transport. *J. Phys. Oceanogr.*, **39**, 1077–1096, https://doi.org/10.1175/2008JPO4044.1.

Huang, C. J., and F. Qiao, 2010: Wave-turbulence interaction and its induced mixing in the upper ocean. *J. Geophys. Res.*, **115**, C04026, https://doi.org/10.1029/2009JC005853.

Jones, N. L., and S. G. Monismith, 2008: The influence of whitecapping waves on the vertical structure of turbulence in a shallow estuarine embayment. *J. Phys. Oceanogr.*, **38**, 1563–1580, https://doi.org/10.1175/2007JPO3766.1.

Kitaigorodskii, S. A., 1983: On the theory of the equilibrium range in the spectrum of wind-generated gravity waves. *J. Phys. Oceanogr.*, **13**, 816–827, https://doi.org/10.1175/1520-0485(1983)013<0816:OTTOTE>2.0.CO;2.

Kukulka, T., A. J. Plueddemann, J. H. Trowbridge, and P. P. Sullivan, 2010: Rapid mixed layer deepening by the combination of Langmuir and shear instabilities: A case study. *J. Phys. Oceanogr.*, **40**, 2381–2400, https://doi.org/10.1175/2010JPO4403.1.

Leibovich, S., 1983: The form and dynamics of Langmuir circulations. *Annu. Rev. Fluid Mech.*, **15**, 391–427, https://doi.org/10.1146/annurev.fl.15.010183.002135.

Li, S., M. Li, G. P. Gerbi, and J.-B. Song, 2013: Roles of breaking waves and Langmuir circulation in the surface boundary layer of a coastal ocean. *J. Geophys. Res. Oceans*, **118**, 5173–5187, https://doi.org/10.1002/jgrc.20387.

Longuet-Higgins, M. S., 1984: Statistical properties of wave groups in a random sea state. *Philos. Trans. Roy. Soc.*, **A312**, 219–250, https://doi.org/10.1098/rsta.1984.0061.

——, and R. W. Stewart, 1962: Radiation stress and mass transport in gravity waves, with application to 'surf beats'. *J. Fluid Mech.*, **13**, 481–504, https://doi.org/10.1017/S0022112062000877.

Lumley, J. L., and E. A. Terray, 1983: Kinematics of turbulence convected by a random wave field. *J. Phys. Oceanogr.*, **13**, 2000–2007, https://doi.org/10.1175/1520-0485(1983)013<2000:KOTCBA>2.0.CO;2.

McWilliams, J. C., J. M. Restrepo, and E. M. Lane, 2004: An asymptotic theory of waves and currents in coastal waters. *J. Fluid Mech.*, **511**, 135–178, https://doi.org/10.1017/S0022112004009358.

——, E. Huckle, J. H. Liang, and P. P. Sullivan, 2012: The wavy Ekman layer: Langmuir circulations, breaking waves, and Reynolds stress. *J. Phys. Oceanogr.*, **42**, 1793–1816, https://doi.org/10.1175/JPO-D-12-07.1.

Noh, Y., H. S. Min, and S. Raasch, 2004: Large eddy simulation of the ocean mixed layer: The effects of wave breaking and Langmuir circulation. *J. Phys. Oceanogr.*, **34**, 720–735, https://doi.org/10.1175/1520-0485(2004)034<0720:LESOTO>2.0.CO;2.

Plant, W. J., 1982: A relationship between wind stress and wave slope. *J. Geophys. Res.*, **87**, 1961–1967, https://doi.org/10.1029/JC087iC03p01961.

Polton, J. A., and S. E. Belcher, 2007: Langmuir turbulence and deeply penetrating jets in an unstratified mixed layer. *J. Geophys. Res.*, **112**, C09020, https://doi.org/10.1029/2007JC004205.

Scully, M., and S. Zippel, 2023: Buzzards Bay Air-Sea Interaction Tower (BB-ASIT) water column data from Fall 2022 deployment. Woods Hole Oceanographic Institution, accessed 19 September 2023, https://doi.org/10.26025/1912/66837.

Scully, M. E., A. W. Fisher, S. E. Suttles, L. P. Sanford, and W. C. Boicourt, 2015: Characterization and modulation of Langmuir circulation in Chesapeake Bay. *J. Phys. Oceanogr.*, **45**, 2621–2639, https://doi.org/10.1175/JPO-D-14-0239.1.

——, J. H. Trowbridge, and A. W. Fisher, 2016: Observations of the transfer of energy and momentum to the oceanic surface boundary layer beneath breaking waves. *J. Phys. Oceanogr.*, **46**, 1823–1837, https://doi.org/10.1175/JPO-D-15-0165.1.

Smith, J., 1983: On surface gravity waves crossing weak current jets. *J. Fluid Mech.*, **134**, 277–299, https://doi.org/10.1017/S0022112083003365.

Soloviev, A. V., N. V. Vershinsky, and V. A. Bezverchnii, 1988: Small-scale turbulence measurements in the thin surface layer of the ocean. *Deep-Sea Res.*, **35A**, 1859–1874, https://doi.org/10.1016/0198-0149(88)90113-6.

Sullivan, P. P., J. C. McWilliams, and W. K. Melville, 2007: Surface gravity wave effects in the oceanic boundary layer: Large-eddy simulation with vortex force and stochastic breakers. *J. Fluid Mech.*, **593**, 405–452, https://doi.org/10.1017/S002211200700897X.

Sutherland, P., and W. K. Melville, 2015a: Field measurements of surface and near-surface turbulence in the presence of breaking waves. *J. Phys. Oceanogr.*, **45**, 943–965, https://doi.org/10.1175/JPO-D-14-0133.1.

——, and ——, 2015b: Measuring turbulent kinetic energy dissipation at a wavy sea surface. *J. Atmos. Oceanic Technol.*, **32**, 1498–1514, https://doi.org/10.1175/JTECH-D-14-00227.1.

Teixeira, M. A. C., and S. E. Belcher, 2002: On the distortion of turbulence by a progressive surface wave. *J. Fluid Mech.*, **458**, 229–267, https://doi.org/10.1017/S0022112002007838.

Terray, E. A., M. A. Donelan, Y. C. Agrawal, W. M. Drennan, K. K. Kahma, A. J. Williams III, P. A. Hwang, and S. A. Kitaigorodskii, 1996: Estimates of kinetic energy dissipation under breaking waves. *J. Phys. Oceanogr.*, **26**, 792–807, https://doi.org/10.1175/1520-0485(1996)026<0792:EOKEDU>2.0.CO;2.

Thomson, J., M. S. Schwendeman, S. F. Zippel, S. Moghimi, J. Gemmrich, and W. E. Rogers, 2016: Wave-breaking

turbulence in the ocean surface layer. *J. Phys. Oceanogr.*, **46**, 1857–1870, https://doi.org/10.1175/JPO-D-15-0130.1.

Veron, F., and W. K. Melville, 2001: Experiments on the stability and transition of wind-driven water surfaces. *J. Fluid Mech.*, **446**, 25–65, https://doi.org/10.1017/S0022112001005638.

Zippel, S. W., J. B. Edson, M. E. Scully, and O. R. Keefe, 2024: Direct observation of wave-coherent pressure work in the atmospheric boundary layer. *J. Phys. Oceanogr.*, **54**, 445–459, https://doi.org/10.1175/JPO-D-23-0097.1.